Bulletin of the Seismological Society of America, Vol. 105, No. 4, pp. 1961–1988, August 2015, doi: 10.1785/0120140330

Ⓔ

Ground-Motion Simulations of 1811–1812 New Madrid Earthquakes, Central United States

by Leonardo Ramirez-Guzman, Robert W. Graves, Kim B. Olsen, Oliver S. Boyd, Chris Cramer, Stephen Hartzell, Sidao Ni, Paul Somerville, Robert A. Williams, and Jinquan Zhong

Abstract We performed a suite of numerical simulations based on the 1811–1812 New Madrid seismic zone (NMSZ) earthquakes, which demonstrate the importance of 3D geologic structure and rupture directivity on the ground-motion response throughout a broad region of the central United States (CUS) for these events. Our simulation set consists of 20 hypothetical earthquakes located along two faults associated with the current seismicity trends in the NMSZ. The hypothetical scenarios range in magnitude from **M** 7.0 to 7.7 and consider various epicenters, slip distributions, and rupture characterization approaches. The low-frequency component of our simulations was computed deterministically up to a frequency of 1 Hz using a regional 3D seismic velocity model and was combined with higher-frequency motions calculated for a 1D medium to generate broadband synthetics (0–40 Hz in some cases). For strike-slip earthquakes located on the southwest–northeast-striking NMSZ axial arm of seismicity, our simulations show 2–10 s period energy channeling along the trend of the Reelfoot rift and focusing strong shaking northeast toward Paducah, Kentucky, and Evansville, Indiana, and southwest toward Little Rock, Arkansas. These waveguide effects are further accentuated by rupture directivity such that an event with a western epicenter creates strong amplification toward the northeast, whereas an eastern epicenter creates strong amplification toward the southwest. These effects are not as prevalent for simulations on the reverse-mechanism Reelfoot fault, and large peak ground velocities (>40 cm/s) are typically confined to the near-source region along the up-dip projection of the fault. Nonetheless, these basin response and rupture directivity effects have a significant impact on the pattern and level of the estimated intensities, which leads to additional uncertainty not previously considered in magnitude estimates of the 1811–1812 sequence based only on historical reports.

The region covered by our simulation domain encompasses a large portion of the CUS centered on the NMSZ, including several major metropolitan areas. Based on our simulations, more than eight million people living and working near the NMSZ would experience potentially damaging ground motion and modified Mercalli intensities ranging from VI to VIII if a repeat of the 1811–1812 earthquakes occurred today. Moreover, the duration of strong ground shaking in the greater Memphis metropolitan area could last from 30 to more than 60 s, depending on the magnitude and epicenter.

Online Material: Tables of 1D velocity models used to generate the high-frequency synthetics, and figures of source models and peak ground motion synthetics.

Introduction

The bicentennial of the New Madrid seismic zone (NMSZ) earthquakes in the central United States (CUS) took place in 2011–2012. This milestone motivated a joint effort that used earthquake simulations to analyze different aspects of the 1811–1812 sequence with recent information and state of the art computational tools. The collaboration targeted three important aspects of these historic events (e.g., Johnston and Schweig, 1996; Hough, 2004; Calais *et al.*, 2010; Hough and Page, 2011): (1) the influence of 3D structures on the ground motion, (2) the potential impacts on today's population in

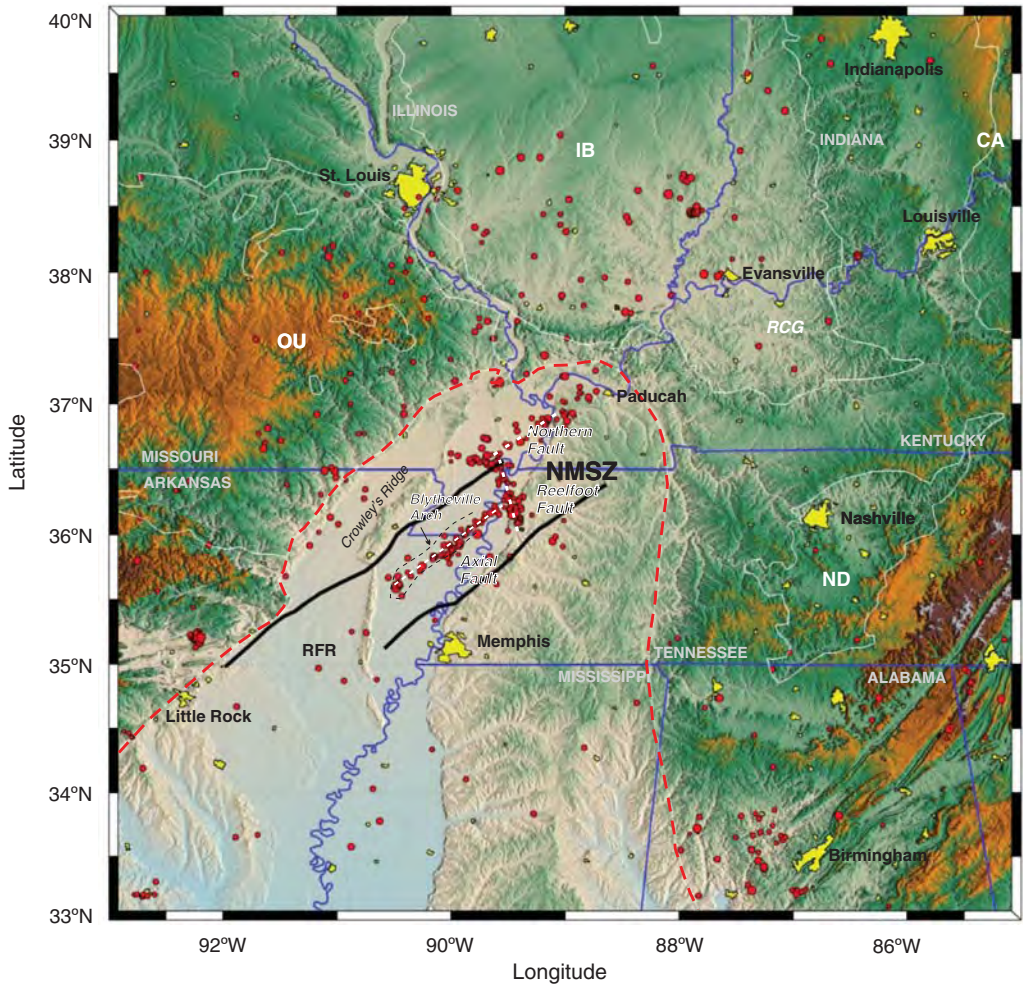

Figure 1. Topographic map showing the extent of the central United States seismic velocity model. Red circles indicate earthquakes greater than magnitude 2.5 that occurred from 1972 to 2010 (the largest earthquake in this time period was the 2008 M_w 5.4 Mount Carmel earthquake in southeastern Illinois). The Mississippi embayment and Reelfoot rift (RFR) boundaries are depicted with red dashed and black continuous lines, respectively. The plausible geometry of three major faults (Northern, Reelfoot, and Cottonwood Grove or Axial) is displayed in white discontinuous line. Some of the geologic structures of the region are also indicated: OU, Ozark uplift; ND, Nashville dome; CA, Cincinnati arch; IB, Illinois basin; RCG, Rough Creek graben.

terms of modified Mercalli intensity (MMI) estimates, and (3) the magnitude uncertainty. This collaboration was built on the experience of similar efforts performed primarily in California (e.g., Aagaard *et al.*, 2008a,b; Bielak *et al.*, 2010) but is unique in its approach, because it explores greater variability in the source characterizations to generate broadband synthetic calculations of the ground motion.

According to several authors (e.g., Nuttli, 1973a,b; Johnston, 1996; Hough *et al.*, 2000; Bakun and Hopper, 2004; Hough and Page, 2011), the three main 1811–1812 earthquakes are among the largest events that have occurred in any of the stable continental regions (SCRs) around the world, as defined by Kanter (1994). The sequence occurred 200 years ago in a sparsely populated region that today is home to several million people. Thus, the importance of the 1811–1812 earthquake sequence bears on the scientific knowledge of intraplate seismicity that these events can provide, its large contribution to the seismic hazard in the CUS (Petersen *et al.*, 2008), and the need to better understand the potentially severe impacts on the built environment that a repeat of this sequence would cause today.

In this study, we examine the ground motion and its macroseismic effects using simulated earthquakes thought to be similar to those of the 1811–1812 sequence on a portion of the CUS centered on the NMSZ (Fig. 1). To perform this task, we employ a recently developed velocity model of the region (Ramirez-Guzman *et al.*, 2010, 2012) and several approaches to generate broadband synthetic seismograms. This 3D velocity model represents a substantial enhancement of the detail and the area covered in previous velocity models of the CUS (Saikia *et al.*, 2006; Macpherson *et al.*, 2010). Three independent methodologies of generating hybrid broadband synthetics are considered. The difference between approaches was encouraged to reveal the variability of the ground motion and provide mean ground motions due to different source characterization and broadband methods.

This article is divided into several sections. We discuss the historic large earthquakes and ground motions from present-day earthquakes in the CUS together with historical accounts and estimated magnitudes of the 1811–1812 sequence. We then present the methodology used to define the source geometry and magnitudes of the three mainshocks of the sequence and the rupture parameters we adopted, as well as a brief description of the approaches employed to generate ground motions for two of the mainshocks. We proceed to analyze the results of the scenarios, focusing on the ground-motion variability and macroseismic effects. Finally, we discuss a preliminary estimate of the magnitude of the events based on our simulations, historical intensity reports, and two ground-motion intensity correlations.

Large Earthquakes in the CUS

Sequences of major earthquakes from the late Holocene provide a compelling reason to study the NMSZ. Geological evidence shows that several earthquake sequences with estimated magnitudes ranging from 7 to 8 took place in the region, with an average recurrence rate of about 500 years (Tuttle *et al.*, 2002). Direct geological evidence of large earthquakes and geophysical images of faulting exist for the NMSZ in the late Pleistocene to early Holocene, but the record is incomplete and poorly constrained earlier than approximately 4000 years ago.

Several models have been proposed to explain the occurrence of earthquakes in the CUS, but there is no scientific consensus regarding the fundamental mechanism responsible for producing them. Liu and Zoback (1997) advocated a thermal weakening of the lower crust and upper mantle, and Pollitz *et al.* (2001) propounded the sinking of a highly mafic body under the NMSZ within a weak lower crust. However, the presence of a weak zone is not supported by the analysis of McKenna *et al.* (2007), which indicates low thermal variations in the CUS. The inferred slip rates during the Holocene on the Reelfoot fault, which are orders of magnitude higher than the average Pleistocene slip rates (Van Arsdale, 2000), led Grollimund and Zoback (2001) to propose a substantial stress field change in and around the NMSZ due to the Laurentide ice sheet melting and thereby inducing higher strain rates. However, Calais and Stein (2009) and Calais *et al.* (2010) concluded that negligible regional strain around the NMSZ is observed from the analysis of Global Positioning System (GPS) data. They argue that the three, possibly four, **M** 7–8 New Madrid earthquake sequences prior to 1811–1812 that occurred in about A.D. 1450, A.D. 900, and A.D. 300 (Tuttle *et al.*, 2002) were transient in nature, and thus conflict with the model used in standard hazard calculations. Frankel *et al.* (2012) found that, after reprocessing the GPS data used by Calais and Stein (2009), the motions recorded in the area are consistent with a finite dislocation slipping at about 4 mm/yr on the Reelfoot fault at 12–20 km depths. A more general treatment by Kenner and Segall (2000) suggests that repeated large-magnitude earthquakes could persist for thousands of years despite the low geodetic surficial motions observed around the NMSZ today.

Although debate about the long-term behavior of the NMSZ exists, there is scientific consensus and concern about a potential repeat of the 1811–1812 sequence, given the earthquake activity over the last few thousand years and the need to understand the damaging ground motions from large earthquakes. Despite the lack of agreement on a model to explain the seismicity, it is important to note that earthquakes are taking place in the region and are not confined to the main seismicity trend of the NMSZ. There are a number of studies that show evidence of Quaternary earthquakes occurring at about a dozen localities around the perimeter of the present-day New Madrid seismicity trends (e.g., Stephenson *et al.*, 1999; Baldwin *et al.*, 2005). However, recurrence times and magnitude estimates have not been extensively studied for most of these localities.

The scientific debate about the meaning of the small observed surface deformation, which has implications for both scientific research and hazard mitigation, is beyond the scope of our present research. We limit the focus of our study to the 1811–1812 earthquake sequence and consider a range of plausible magnitudes and the potential earthquake ground motions of the two largest earthquakes from this sequence.

Ground Motion in the CUS

Even though recorded ground motions of medium-to-large magnitude earthquakes are scarce in the central and eastern United States (CEUS), several observations about the ground motions, ground-motion parameters, and macroseismic MMIs have been documented. Henceforth, we will use the terms "intensity" and "MMI" interchangeably. These observations are crucial to evaluate our simulations as plausible realizations of earthquakes taking place in the NMSZ.

Evernden (1967) and Nuttli (1973a) developed attenuation relations for the region and were most likely the first to show that ground-motion attenuation in the CEUS is substantially lower than it is in the western United States. The felt areas for the same magnitude event are larger in the CEUS than in the west. Several authors derived intensity prediction equations (IPEs) for the CEUS that equate MMI to a function of epicentral distance and moment (Bakun *et al.*, 2003; Bakun and Hopper, 2004; Atkinson and Wald, 2007; Boyd and Cramer, 2014), many of which were used in the latest magnitude estimations of historic earthquakes in the area (Bakun and Hopper, 2004; Hough and Page, 2011; Boyd and Cramer, 2014). The reported median distance for $M_w < 5.5$ earthquakes and felt intensities of IV would not be expected to exceed ~100 km in California (Bakun and Wentworth, 1997), whereas in the CEUS the reported median distance is expected to be closer to ~400 km (Fig. 2).

Predictive relationships between MMI and ground-motion parameters or ground-motion intensity correlation equations (GMICEs) for the CEUS have been proposed (e.g., Kaka and Atkinson, 2004; Atkinson and Kaka, 2007; Dangkua and Cramer, 2011). In most cases, it is clear that earthquakes are perceived differently in the west and east, which may be due to the prevalence of medium and large magnitude earthquakes

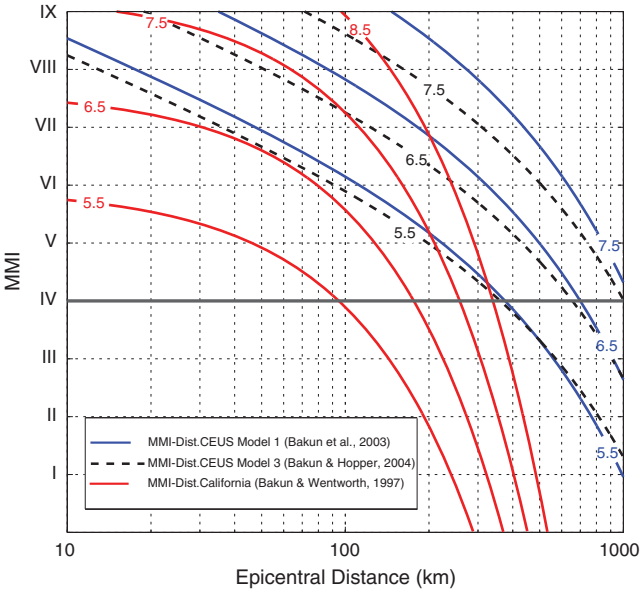

Figure 2. Central and eastern United States (CEUS) and California attenuation. Intensity-magnitude–distance curves for California are displayed as a continuous red line for **M** 5.5, 6.5, 7.5, and 8.5. Models 1 and 3 for CEUS, following the Bakun and Hopper (2004) convention, are plotted with blue continuous and black discontinuous lines for **M** 5.5, 6.5, and 8.5. The median distances for felt intensities of IV would not be expected beyond ~100 km for $M_w < 5.5$ earthquakes in California, whereas, in the CEUS, median distances are expected to be ~400 km.

in the west, high-Q crustal structure in the east, or different structural vulnerabilities and building practices. Current risk analysis at regional and local level uses more assertive instrument-based intensity metrics than MMI (see e.g., Riddell, 2007; Campbell and Borzorgnia, 2012). Nevertheless, MMI is a good first-order estimate of the earthquake effects when they are computed using numerical simulations and appropriate GMICEs, as presented in this research, and provides one of the few parameters to study pre-instrumental seismicity.

Atkinson and Boore (1995, 2006) developed ground-motion prediction equations (GMPEs) using synthetic ground motions based on point-source and stochastic finite-fault methodologies (e.g., Boore, 1983; Motazedian and Atkinson, 2005) for eastern North America. The GMPEs have three distinct distance regions: a steep near-source attenuation region, a transition zone with a subtle attenuation, and a region that exhibits high fall-off at longer distances. Pezeshk *et al.* (2011) used a hybrid empirical method to produce comparable results with those proposed by Atkinson and Boore (2011) for distances greater than 10 km at all magnitudes but with lower attenuation at distances close to the source. Several researchers note that in regions where 3D structures are important, such as the Mississippi embayment, the GMPEs only offer a reference level (e.g., Dorman and Smalley, 1994; Bodin and Horton, 1999; Street *et al.*, 2001; Langston *et al.*, 2006; Macpherson *et al.*, 2010; Hartzell and Mendoza, 2011; Ramirez-Guzman *et al.*, 2012).

GMPEs cannot accurately account for basin or directivity effects. As a result, we chose to generate hybrid broadband ground motions and made use of full 3D simulations in the CUS for frequencies lower than 1 Hz. These better constrain the ground-motion variability and provide insights into the wave propagation. When used together with ground motions, they are suitable for higher frequencies as well. In our simulations, basin and directivity effects appear to provide potentially important insights into the ground motions of the 1811–1812 earthquakes. A comparison of a GMPE and the ground-motion simulations is presented in this study.

Some previous work on 3D numerical earthquake simulations has been done in the NMSZ. For instance, Saikia *et al.* (2006) presented an analysis of simulations using 1D, 2D, and simple 3D structures of the Mississippi embayment. The minimum S-wave velocity (V_S) was 600 m/s, and the results suggested that the effects of the deep structure below the sediments had little impact on the long-period ground-motion amplitudes ($T \geq 2$ s) for earthquakes taking place in the central part of the embayment. Macpherson *et al.* (2010), using a model with improved geologic structural constraints and minimum $V_S = 600$ m/s, concluded that not only do finite-fault effects such as directivity, slip distribution, and fault proximity exert the most control on ground motions, but so too does the 3D geologic structure of the upper Mississippi embayment. In addition, there are indications that ground-motion amplification can be caused by the sharp seismic velocity contrast at the basin edge. Our simulations build on this work by incorporating well-constrained structural features in a broader region of the CUS, refinements such as lower minimum V_S (360 m/s in some scenarios), robust source models, and higher-frequency resolution than any previous study.

The 1811–1812 New Madrid Sequence and Magnitude Estimates

Three principal events and a large aftershock dominated the winter of 1811–1812 New Madrid earthquake sequence. The series of earthquakes started on the morning of 16 December 1811 (~2:15 a.m. local time) when the inhabitants of the New Madrid area and over most of the United States—at the time of the earthquakes the New Madrid area was a sparsely inhabited region and the United States consisted of states east of the epicenters—were abruptly awakened by the cracking, groaning, and rattling of furniture and timber in their homes and other structures (Fuller, 1912; Johnston, 1996). Contemporary accounts document a severe aftershock early on the morning (~2:15 a.m. local time) of 16 December 1811, and two additional mainshocks on 23 January and 7 February 1812 (~9:15 a.m. and ~3:45 a.m. local time, respectively), followed by a year of smaller but noticeable shocks (Fuller, 1912; Hough, 2004). Each of the three mainshocks was followed by an energetic aftershock sequence, including several in the **M** 6.0–6.3 range (Hough, 2009). Henceforth, we will refer to the three principal events in December, January, and February as NM1, NM2, and NM3, respectively, following Johnston (1996) and Hough (2004).

The dramatic historical accounts of the impact of the earthquakes on the settlements near the epicentral area and

the Mississippi River—especially those about geysers of sand and mud (sand blows) as tall as trees, the river flowing backward, and the creation of temporary waterfalls on the Mississippi River (Fuller, 1912)—test the credibility of the eyewitness testimonies. However, the consistency and number of these accounts, as well as the extent of the large 1811–1812 sand blow field still visible today, with individual sand blows observed to be large compared with sand blows worldwide (Tuttle *et al.*, 2002), supports a plausible scenario of very strong and prolonged shaking occurring in the area that is difficult to diminish. Felt reports of these earthquakes exist as far north as Canada and were documented extensively by the population of the east coast of the United States (distances up to 1700 km). These reports, together with the extensive area of liquefaction, landslides, and changes in the geomorphology of the region, provide some constraints on the size and possible consequences of a similar sequence.

Several researchers studied the magnitude of these earthquakes (Table 1). Nuttli (1973b) made the first assessment of the mainshocks by giving magnitude and ground-motion estimates. These early assessments, m_{Lg} 7.1, 7.2, and 7.4 for NM1, NM2 and NM3, respectively, were based on the recorded ground motion of the 9 November 1968 Illinois earthquake and other earthquakes in eastern North America, together with the interpretation of MMI values from newspaper reports of the severity of the earthquakes throughout the CEUS. Gomberg (1992) suggested $M_w \sim 7.3$ for the NM1 event by analyzing the seismicity and tectonic deformation. Later, Johnston (1996) obtained M_w values ranging from 7.8 to 8.1 based on an isoseismal approach of interpreted MMI. Following the method described in Johnston (1996), Hough *et al.* (2000) reexamined the felt reports and reduced several MMI assignments because of suspected site amplification. The analysis indicated lower-magnitude values, from 7.0 to 7.5, for the sequence of mainshocks. Bakun and Hopper (2004), using the method of Bakun and Wentworth (1997) with MMI–distance relationships derived from data collected by Bakun *et al.* (2002) and Bakun *et al.* (2003) MMI assignments, computed magnitudes from 7.5 to 7.8, higher than those reported by Hough *et al.* (2000). In contrast to the isoseismal approach, the method used by Bakun and Wentworth (1997) is based on individual intensity reports, which reduce the uncertainty of the estimation. More recently, Hough and Page (2011) reevaluated the Bakun and Hopper (2004) work using MMI values interpreted by four different experts and using the same attenuation models derived with the original Bakun *et al.* (2003) MMI data. The magnitude estimates were substantially lower than any previous assessment, ranging from 6.5 to 7.3, which added to the debate about the seismic hazard on the NMSZ.

Bakun and Hopper (2004) assumed that the Bakun *et al.* (2003) MMI data, used to obtain the attenuation relationships employed in their magnitude assignments, followed Wood and Neumann (1931). The latter is an assumption that is hard to guarantee due to the subjectivity involved in the MMI assignments. Thus, there is a fundamental source of uncertainty in both estimations (Bakun and Hopper, 2004; Hough and Page, 2011), because the MMI interpretation is not unique.

Table 1
Moment Magnitude Determinations by Different Authors

Author	NM1 (16 December) Southern Segment	NM2 (23 January) Northern Segment	NM3 (7 February) Central Segment
Nuttli (1973a)	7.7*	7.5*	7.9*
	8.1†	7.9†	-†
Gomberg (1992)	7.3	-	-
Johnston (1996)	8.1	7.8	8.0
Hough *et al.* (2000)	7.2–7.3	7.0	7.4–7.5
Bakun and Hopper (2004)	7.6	7.5	7.8
Hough and Page (2011)	6.7–6.9	6.5–7.0	7.1–7.3

*The value was computed using the original Nuttli (1973a) m_b/m_{Lg} using Johnston (1996) regressions for m_{Lg} and M_s.

†Value computed using the Nuttli (1973a) m_b/m_{Lg} but using the Sipkin (2003) m_b to M_w; the m_b/m_{Lg} 7.4 of NM3 was not converted because Sipkin's regression is not valid beyond m_b 7.3.

More recently, considering additional "Did You Feel It?" intensity data and historical distributions of population, Boyd and Cramer (2014) developed a new IPE and used multiple intensity datasets to infer moment magnitudes between 6.9 and 7.6 for the three New Madrid mainshocks. Cramer and Boyd (2014) used far-field intensity comparisons with two recent large-magnitude intraplate earthquakes to estimate magnitudes between 7.3 and 7.7. In this research, we take advantage of our simulated ground motions and examine the magnitude range of NM1 and NM3, assuming that our mean ground motions are plausible representations of the 1811–1812 sequence effects.

This study models the NM1 and NM3 events. To focus our discussion on the two largest events, the analysis of the NM2 event is not included in this article. (Ⓔ Some results for NM2 can be found in the electronic supplement to this article.)

Methodology

Our ground-motion simulations use the Central United States Velocity Model (CUSVM) v.1.2 (Ramirez-Guzman *et al.*, 2010, 2012), three different source generators, three different seismic wave propagation codes, and three broadband generation approaches. Earlier versions of the wave propagation codes were verified in previous exercises (e.g., Bielak *et al.*, 2010). We performed a new verification, summarized in the Appendix, to guarantee that the code's versions give similar results. Once the three solving platforms were verified, the geometry of the faults and magnitudes for NM1 and NM3 were defined using appropriate scaling relationships. We modeled two fault planes and four magnitudes. A total of 20 kinematic and dynamic rupture models were generated and simulated. We analyzed the ground-motion variation between scenarios, the influence of 3D structures, the population exposed to various MMI levels around the NMSZ, and the mag-

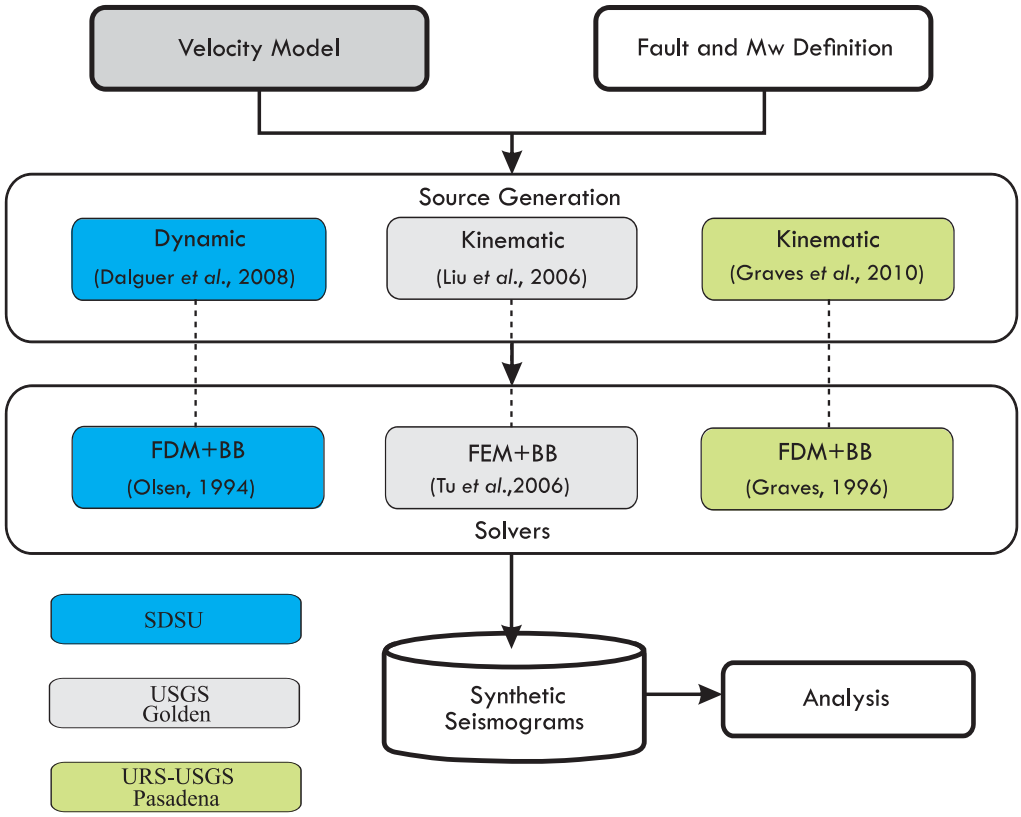

Figure 3. Collaboration scheme. Activities performed per group at (blue) San Diego State University (SDSU), (gray) U.S. Geological Survey Golden (USGSG) and (green) URS–USGS-Pasadena. FDM, finite-difference method; FEM, finite-element method; BB, broadband.

nitude uncertainty of NM1 and NM3. Figure 3 displays the general overview of the collaboration.

Velocity Model

We used the CUSVM v.1.2 in the collaboration. It is very similar to v.1.3, described in Ramirez-Guzman *et al.* (2012). The model represents a compilation of decades of crustal research consisting of seismic, aeromagnetic and gravity profiles, geologic mapping, geophysical and geological borehole logs, and inversions of the region's seismic properties. The density, *P*- and *S*-wave velocities are synthesized in a stand-alone spatial database that can be queried to generate the required input for numerical seismic-wave propagation simulations. Figure 4 displays cross sections at selected locations in the area of interest for v.1.2. In the latest version of the model (v.1.3; see Data and Resources), some modifications on the unit boundaries that define the deep structure were included, as well as velocities from analysis of seismic reflection lines in the region around the NMSZ. A constraint of $V_S > 3.4$ km/s was imposed in Precambrian materials to improve the fit of surface-wave arrival-time observations for the 2008 M_w 5.4 Mount Carmel, Illinois, earthquake. In addition, some of the velocities in the post-Paleozoic section of the Mississippi embayment were modified in light of newly available information. Nevertheless, the ground motions obtained between versions 1.2 (used in this research) and 1.3 are not significantly different and do not affect the conclusions presented here.

Wave Propagation Codes and Verification

Three groups simulated the wave propagation: (1) Olsen and Zhong or San Diego State University (SDSU), (2) Ramirez-Guzman, Hartzell, Boyd, and Williams or U.S. Geological Survey Golden (USGSG), and (3) Graves, Ni, and Somerville or URS Corporation and U.S. Geological Survey Pasadena (URSUSGSP). The codes used were developed over the course of several years (Graves, 1996; Olsen and Archuleta, 1996; Tu *et al.*, 2006) and are able to solve the elastodynamic equations in large 3D heterogeneous media. All codes have second-order accurate temporal schemes. The two staggered-grid finite-difference codes used by SDSU and URSUSGSP have fourth-order spatial convergence. In contrast, the unstructured octree-based finite-element toolchain used by USGSG has second-order spatial convergence. Bielak *et al.* (2010) present a verification among the codes for one of the California ShakeOut scenarios. The codes are able to reproduce practically the same ground motion when the earthquake source, frequency content, mesh, and exact comparison location are clearly specified and implemented. In this collaboration, we decided to test the codes again, because they have been modified and the velocity model used was recently developed. The Appendix summarizes a suc-

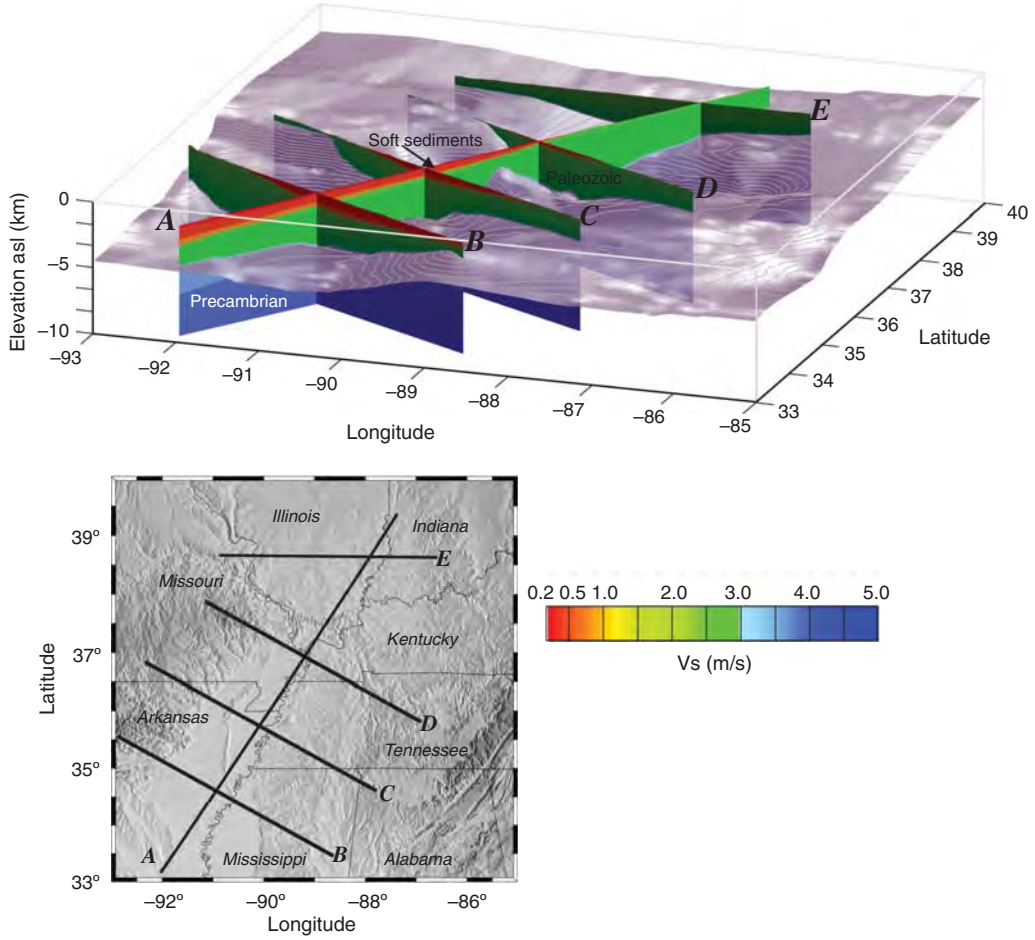

Figure 4. Central United States Velocity Model (1.2). Fence model where cross sections display the *S*-wave velocity (asl, above sea level). The Precambrian unconformity is displayed in gray. The lower left panel indicates the location of the cross sections displayed.

cessful verification using the source mechanism and slip function of the 18 April 2008 M_w 5.4 Mount Carmel, Illinois, earthquake as an input source.

Broadband Synthetics Generation

To extend the frequency range of the synthetic ground motion, three hybrid methods are used to combine the 3D low-frequency finite-difference/finite-element and high-frequency synthetics. In two of them, USGSG and URSUSGSP, the low- and high-frequency synthetics were combined using a matched filter method with a crossover frequency of 1 Hz. A 1D layered velocity model (see Ⓔ electronic supplement) was used by USGSG to generate synthetics using the method of Zhu and Rivera (2002), which were summed to simulate rupture on a finite fault following the method of Liu *et al.* (2006). The URSUSGSP used the hybrid broadband method of Graves and Pitarka (2010). The high-frequency synthetics were generated using a semistochastic approach, where simplified Green's functions were calculated for two 1D velocity models—one for Mississippi embayment sites and the other for the rest of the simulated domain (see Ⓔ electronic supplement). The third hybrid approach, used by SDSU, generates broadband ground motions using the hybrid approach by Mai *et al.* (2010) and Mena *et al.* (2010), which is based on a multiple shear-to-shear (*S*-to-*S*) backscattering theory (Zeng *et al.*, 1991) and a simultaneous amplitude and phase-matching algorithm (Mai and Beroza, 2003).

NMSZ Source Constraints

The geometry of the three major New Madrid faults (Cottonwood Grove or Axial, Reelfoot, and Northern; Fig. 1), thought to have been responsible for earthquake sequences in the past, have been delineated on the basis of seismicity recorded since the mid-1970s (Stauder *et al.*, 1976; Andrews *et al.*, 1985; Chiu *et al.*, 1992; Csontos and Van Arsdale, 2008; Dunn *et al.*, 2010).

As described earlier, there is no agreement on the exact location and magnitudes of the mainshocks in the 1811–1812 sequence. The epicenters proposed by Bakun and Hopper (2004) and Hough and Page (2011) for the 1811–1812 mainshock earthquakes are shown in Figure 5, together with a set of recent relocated earthquakes with the three characteristic central, southern, and northern seismicity trends or segments (Chen *et al.*, 2006). The southern and central segments

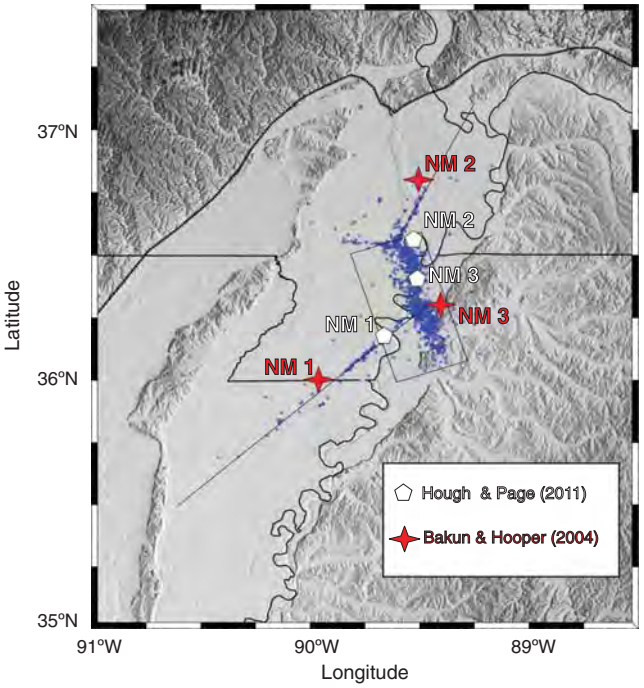

Figure 5. Epicentral location of the 1811–1812 mainshocks. Locations for NM1 (16 December 1812), NM2 (23 January 1812), and NM3 (7 February 1812) according to Bakun and Hopper (2004) and Hough and Page (2011), indicated by stars and pentagons, respectively. Relocated seismicity is shown in blue circles and proposed planes for the M_w 7.7, 7.4, and 7.6 earthquakes for NM1, NM2, and NM3, respectively.

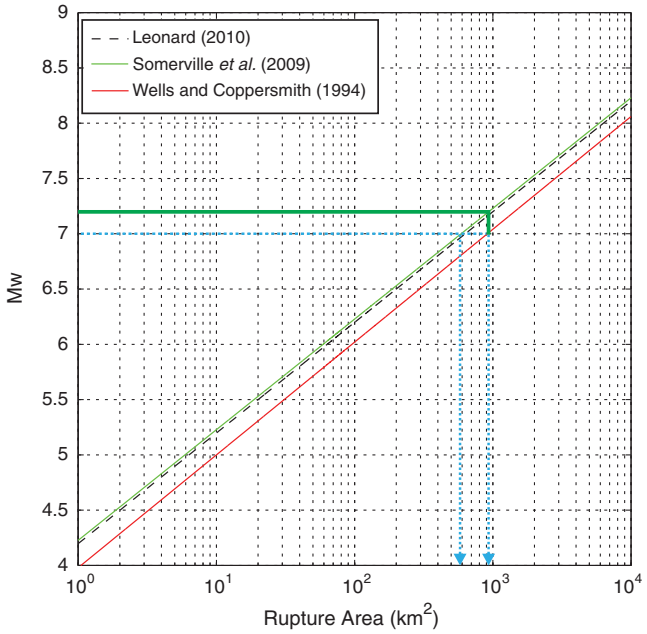

Figure 6. M_w–area relationships. Wells and Coppersmith (1994) relationship, displayed in red, is compared against two stable continental region relationships, Leonard (2010; black dashed line) and Somerville *et al.* (2009; green). Wells and Coppersmith (1994) require larger areas for a given M_w compared with the other two relationships. The blue discontinuous lines exemplify the case of an M_w 7 earthquake, in which an area of ~900 km^2 is predicted with Wells and Coppersmith (1994) and ~600 km^2 with the other two, a 1.5 ratio.

are also known as the Cottonwood Grove (or Axial) and Reelfoot faults, respectively. We will use these names interchangeably throughout the document.

The seismicity and magnitude range proposed by different authors provide some constraints on the minimum lengths and areas that the earthquake source could have, assuming that a moment and area relationship is available. Several source-scaling relationships have been published (e.g., Wells and Coppersmith, 1994; Somerville *et al.*, 1999; Hanks and Bakun, 2008; Leonard, 2010; Yen and Ma, 2011) for global datasets or tectonically differentiated regions. The most widely used source-scaling relationships to define geometric characteristics, especially the moment–area relationship, of probable earthquake scenarios are those given by Wells and Coppersmith (1994), which are based on a large set of faulting parameters for continental earthquakes. However, studies have found that these relationships underestimate the moment, given the area for earthquakes larger than **M** 7 (Hanks and Bakun, 2008; Shaw, 2009) or in SCR earthquakes (Somerville *et al.*, 2009; Leonard, 2010). In Figure 6, we display the moment–area relationships by Wells and Coppersmith (1994), Somerville *et al.* (2009), and Leonard (2010). The last two were specifically developed for SCR such as CUS and give similar values. In contrast, the Wells and Coppersmith (1994) equation predicts, for the same magnitude, rupture areas ~1.5 times larger than the SCR relationships.

We use the SCR relationships and fault geometries that honor the observed seismicity. The resulting fault planes, including the rupture dimensions, are displayed in Table 2 and Figure 7. We assume that modern seismicity trends are a good indicator of the 1811–1812 seismogenic zone and that NM1 and NM3 occurred in the southern and central segments, respectively, and NM2 in the northern segment. The fault area was defined based on the Leonard (2010) SCR moment to area relationship, and fault width and length were fixed to encompass the observed seismicity, and considering hypocentral locations. In accordance with Csontos and Van Arsdale (2008), we assumed that the Cottonwood Grove and northern faults have right-lateral strike-slip motion on nearly vertical fault planes, whereas the Reelfoot fault is characterized by a thrust motion. These fault planes and the three upper and two lower magnitudes associated within each of the seismicity trends are intended to explore the potential range of ground motions using, at the low end, the magnitudes proposed by Hough and Page (2011) and, at the high end, those used for New Madrid in the 2008 USGS probabilistic National Seismic Hazard Maps (Petersen *et al.*, 2008, 2014). Here, we focus our attention only on NM1 and NM3, and leave NM2 for future studies.

Except for Johnston (1996), the NM3 event is considered the largest event, which, as noted by Hough and Page (2011), is contradictory to the number of reported felt intensities (NM3 has half the number of those for NM1). In agreement with Johnston (1996), the largest magnitude in this

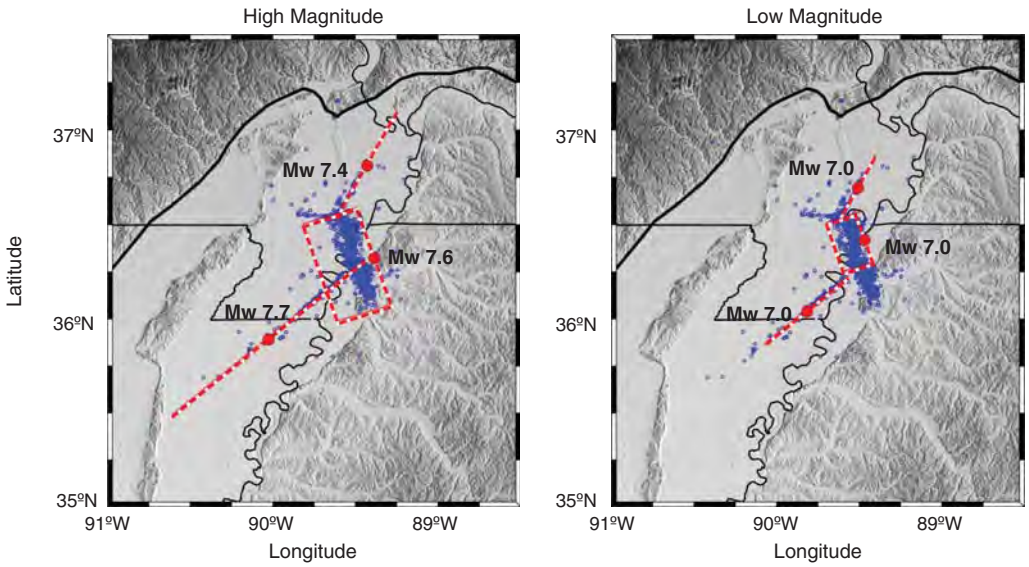

Figure 7. Fault geometry for the scenarios. (left) Surface-projected fault geometries of the high-magnitude scenarios M_w 7.4, 7.6, and 7.7 for the northern, central, and southern segments indicated with red discontinuous line. (right) The low-magnitude scenarios.

study (M_w 7.7) is assigned to the southern segment (NM1), and our minimum magnitudes are M_w 7.0.

Earthquake Source Generation

The SDSU group generated earthquake-source representations using a fully dynamic approach (Dalguer *et al.*, 2008). The resulting slip rate at each node was projected onto the fault and then simulated as a kinematic source. The rupture generation was established under heterogeneous initial conditions for thrust and strike-slip faults for a given M_w considering a depth-dependent stress and initial shear stress following fractal distributions. A linear slip-weakening friction law was used.

In the URSUSGSP case, the source was generated using the procedure described in Graves and Pitarka (2010). The slip distribution was based on Mai and Beroza (2002), with an average rupture velocity V_r = 80% of the local V_S and timing perturbations that scale with local slip; higher slip implies faster rupture. The rise time used in the model considers the empirical analysis of Somerville *et al.* (1999), in which average rise times are 1.85 longer than the active tectonic regions, with subfault values scaling with the square root of local slip. Rupture velocity was decreased by a factor of 0.7 and rise time was increased by a factor of 2 within 5 km of the ground surface.

The USGSG group used a modified version of the approach described by Liu *et al.* (2006). This method uses the notion of correlated random source parameters; slip, rupture velocity, and rise time are represented as random correlated variables. The slip distribution was defined considering correlation lengths within one standard deviation of the mean values proposed by Mai and Beroza (2002). A correlation $V_{r-Slip} = -0.05$ with average rupture velocity of $0.8V_S$ was used. To remove unrealistically large ground-motion values of velocity near the source, the rupture time was lengthened using a 1D velocity model that accounts for very low *S*-wave velocities near the surface. Further reduction in surficial ground-motion velocities was achieved by linearly tapering the rupture velocity (V_r), rise time (T_r), and slip starting from a zero value at the fault's top to the value obtained at 5 km depth down dip with the procedure outlined above.

Examples of the source rupture models generated for the southern segment (NM1) are shown in Figure 8 (see Ⓔ electronic supplement for the entire set). Some differences are clear in the two unilateral kinematic ruptures for the large magnitude case M_w 7.7. In the case of the USGSG model, the rupture progressed with a subtly slower rupture velocity than in the case of the URSUSGSP rupture, which in contrast had larger rise times. In both cases, the rake had a fairly large varia-

Table 2
Source Description, Magnitude, and Geometrical Characteristics

Segment (Event)	Top Center (Longitude, Latitude, Depth)	L (km)	W (km)	Strike, Dip, Rake	M_w (Leonard, 2010)	M_w (Simulations)
Southern (NM1)	(−90.0273, 35.9036, 0)	140	22	229, 90, 180	7.68	7.7
Southern (NM1)	(−89.8579, 36.0230, 4)	60	11	229, 90, 180	7.01	7.0
Central (NM3)	(−89.3830, 36.3386, 0)	60	40	162, 38.7, 90	7.57	7.6
Central (NM3)	(−89.4644, 36.4356, 3)	30	22	162, 38.7, 90	7.01	7.0

Figure 7 depicts the proposed fault geometry of the different segments; depth is in kilometers.

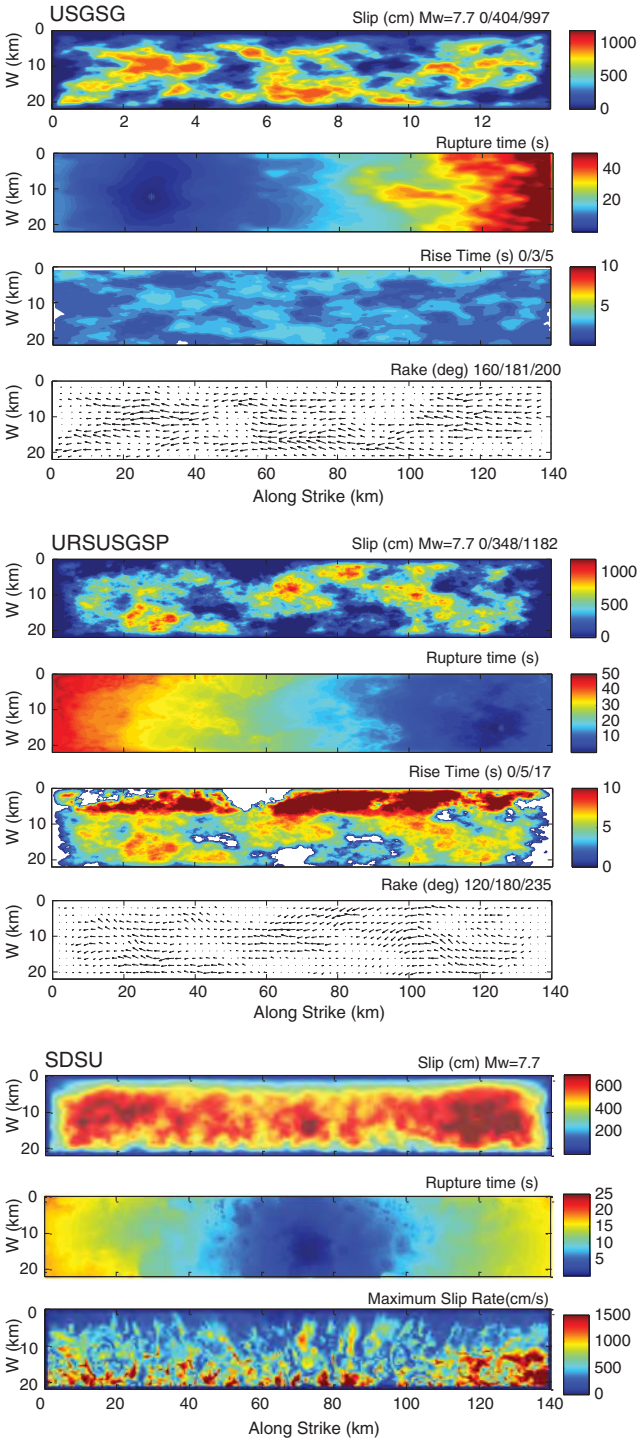

Figure 8. Source parameters for the M_w 7.7 southern segment simulation. Three examples, one per simulation group, are displayed. The kinematic ruptures in the U.S. Geological Survey Golden (USGSG) and URS Corporation and U.S. Geological Survey Pasadena (URSUSGSP) simulations display slip, rupture time, rise time, and rake in the subfaults. The source derived from a dynamic rupture simulation is displayed in the last three panels (SDSU), in which the slip, rupture time, and maximum slip rates are shown.

tion. On the other hand, the source constrained by a fully dynamic rupture procedure did not show as much incoherency in the slip distribution as in the kinematic cases, but had similar rupture time variation. The maximum slip rate for the SDSU source was concentrated in the bottom middle of the fault, which was consistent with the kinematic rupture approaches. The URSUSGSP case had slightly more asperities than in the USGSG model, which had little variation in the rise time and most of the slip located on the bottom half of the fault.

A total of 20 scenarios were simulated in this collaboration, with an emphasis on earthquakes occurring in the central and southern segments (see Ⓔ electronic supplement for the entire set and additional simulations including the northern segment).

Ground-Motion Simulations

The three simulation groups chose a regional crustal volume considered to be sufficiently large and constrained the minimum shear-wave velocity such that 625 m/s were used by URSUSGSP, 500 m/s by SDSU, and 360 m/s by USGSG. The simulated regions for each group are summarized in Table 3, together with the characteristics of the simulation parameters (see Ⓔ electronic supplement for the entire set). The number of simulations per group is listed in Table 4.

Results

Ground-Motion Variability

Southern Segment Rupture Simulations: Cottonwood Grove Fault (NM1). To explore the differences between the broadband ground motions generated by each group, which in the cases of SDSU and USGSG were only at selected stations, in Figure 9 we display the synthetic velocity and smoothed Fourier amplitude spectra for three bilateral M_w 7.7 earthquakes in the southern segment generated by each group. The highest frequency bands are 5, 10, and 40 Hz for USGSG, SDSU, and URSUSGSP, respectively. All stations are located in the Mississippi embayment (Fig. 10a). In general, the ground motions predicted in low frequency (< 1 Hz) by USGSG and SDSU are higher than those computed by URSUSGSP, which is expected due to the lower velocities employed by the first two groups in that frequency range. Even though the shape of all synthetics is very similar at each station, ground-motion parameters such as duration and response spectral accelerations would be different. The differences among modelers—all due to sources and broadband synthetics methods with reasonable but different assumptions—were encouraged in the collaboration. A thorough study of the methods is not an objective of the present research, but efforts to document and analyze source and broadband generation methods are a very active area of research today (e.g., Goulet *et al.*, 2015, and references therein).

A regional perspective on the ground-motion variability due to earthquakes in the southern or Axial segment is illustrated in Figure 10, where we present the horizontal root mean square peak ground velocity (PGV) for three M_w 7.7 (Fig. 10a–c) and

Table 3
Description of the Simulations

Simulation Group	SDSU	USGSG	URSUSGSP
Domain			
Length (km)	560	390	360
Width (km)	400	520	190
Depth (km)	60	65	65
Southwest	−91.6877, 34.6820	−91.50000, 34.50000	−90.24323, 34.47712
Northwest	−91.6039, 39.7403	−91.63374, 39.18452	−91.80949, 35.60080
Northeast	−87.3813, 39.7380	−87.11942, 39.18452	−89.13155, 38.02031
Southeast	−87.3610, 34.6827	−87.25317, 34.50000	−87.55619, 36.86156
Projection	UTM	Bilinear	Spheroidal
Discretization			
Space	Staggered-grid FD Fourth order	Octree-based FE Second order	Staggered-grid FD Fourth order
Time	Second order	Second order	Second order
Resolution			
Cell or element size	100 m	Variable	125 m
F_{max} (Hz)	L-F 1.0 (10.0 Hz at some stations)	L-F 1.0 (5.0 Hz at some stations)	BB 40.0 Hz
Minimum V_S (m/s)	500	360	625
Points per S wavelength	5	8	5
Attenuation			
Type	Coarse grained	Rayleigh	Coarse grained
Q_S	$0.300V_S - 100$ $600 \le V_S \le 1000$ $0.167V_S + 33$ $1000 \le V_S \le 4000$ 700 $4000 \le V_S$	-	$0.300V_S - 100$ $600 \le V_S \le 1000$ $0.167V_S + 33$ $1000 \le V_S \le 4000$ 700 $4000 \le V_S$
Q_P	$2Q_S$	-	$2Q_S$
Q	-	$0.300V_S - 100$ $600 \le V_S \le 1000$ $0.167V_S + 33$ $1000 \le V_S \le 4000$ 700 $4000 \le V_S$	-
Absorbing Boundaries			
Type	Perfectly matched layers	Lysmer–Kuhlemeyer	Clayton–Engquist

BB, broadband, L-F, low frequency; FD, finite difference; FE, finite element; SDSU, San Diego State University or Olsen and Zhong; USGSG, U.S. Geological Survey Golden, Colorado or Ramirez-Guzman *et al.*; URSUSGSP, URS Corporation and U.S. Geological Survey Pasadena, California, office or Graves *et al.* V_S is given in meters per second.

two M_w 7.0 (Fig. 10d,e) earthquakes on the segment, with different epicenters. Except for URSUSGSP (maximum frequency 40 Hz), the ground motions are valid up to 1 Hz (see Ⓔ electronic supplement for the entire set). In the same figure, we include peak ground acceleration (PGA), PGV, and response spectral acceleration (SA) at $T = 2$ s attenuation curves.

Table 4
Magnitude and Number of Simulations per Fault Performed by Group

Segment (Event)	Magnitude (M_w)	USGSG	URSUSGSP	SDSU	Total
Southern (NM1)	7.7	3	3	3	9
	7.0	2	1	-	3
Central (NM3)	7.4	2	2	2	6
	7.0	1	1	-	2

SDSU, San Diego State University or Olsen and Zhong; USGSG, U.S. Geological Survey Golden, Colorado or Ramirez-Guzman *et al.*; URSUSGSP, URS Corporation and U.S. Geological Survey Pasadena, California, office or Graves *et al.*

Generally, SDSU and USGSG estimate larger values of PGV and SA ($T = 2$ s) than the URSUSGSP team. URSUSGSP, with broad frequency content, estimates higher PGA values than the other two groups. For reference, in Figure 10 we also plot the ground-motion parameters as a function of distance for the simulations against the Pezeshk *et al.* (2011) GMPE for PGA and SA ($T = 2$ s) without any additional site correction for lower velocities than those considered (National Earthquake Hazards Reduction Program site class A, $V_{S30} \ge 2000$ m/s) by Pezeshk *et al.* (2011). Including higher frequencies in the synthetics (URSUSGSP) produces PGA values compatible with the GMPE shown. Nevertheless, near the source (< 10 km) PGA attenuation is similar to or more gradual than in the GMPE. The ratio between the median value for URSUSGSP simulations and the prediction equation is approximately 0.67. The lower PGA values (with respect to the GMPE) predicted by SDSU and

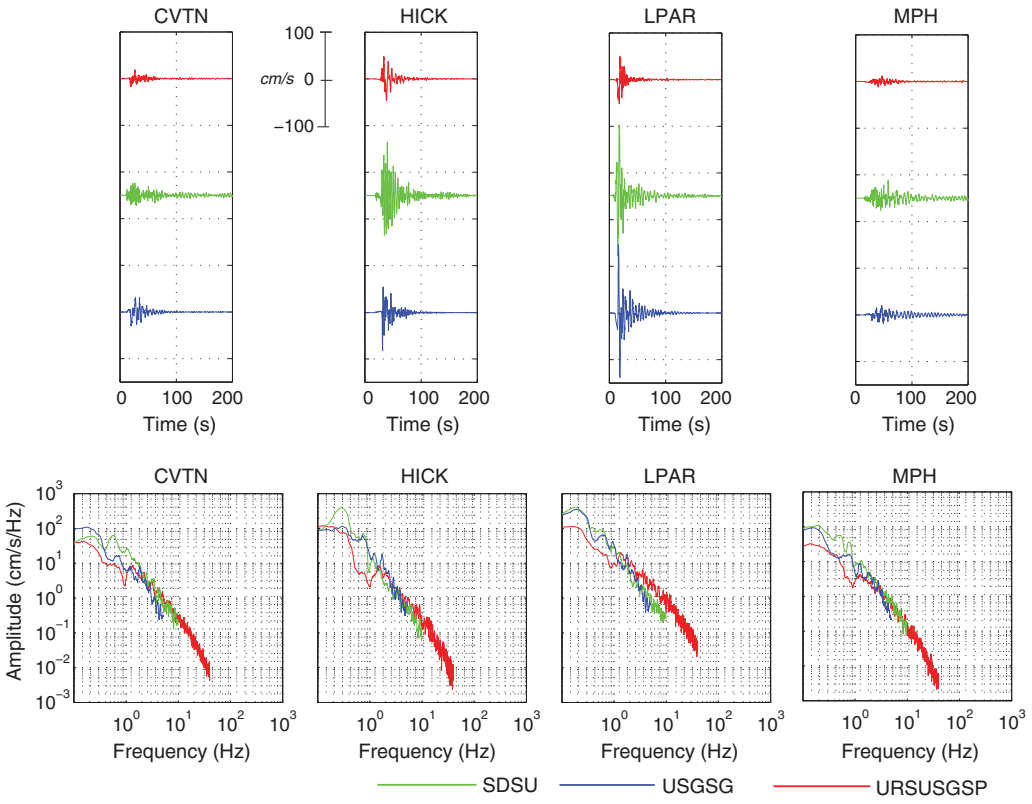

Figure 9. Broadband synthetic seismograms: (top) velocity time histories for the three simulation groups for an M_w 7.7 scenario in the southern segment with bilateral rupture, and (bottom) corresponding velocity Fourier spectra for all synthetic signals.

USGSG are due to limited frequency content. For distances <100 km, the GMPE-to-median-ground-motion ratio in the aforementioned cases is approximately 2; beyond 100 km, the ratio can reach values close to 3.5. The latter highlights the importance of the high-frequency (>1 Hz) energy in the PGA.

Regarding the median response SA for $T = 2$ s (5% damping), the values obtained in the simulations are higher than the corresponding GMPE values, mainly due to amplification caused by *S*-wave velocities included in the low-frequency simulations. Taking the GMPE as reference, amplification factors of 2–3 and 4–7, are observed for URSUSGSP and the other two groups, respectively, which are in agreement with the minimum *S*-wave velocities modeled.

In all simulations with M_w 7.7, the trend of the PGA and PGV does not show any drastic change within 100 km. A $1/R^{\alpha}$ (with α slightly larger than 1) geometric spreading factor for distances <100 km can be used to model our calculations, and beyond 100 km α can have values <1. In contrast, the tendency of the SA ($T = 2$ s) attenuation in several simulations changes at distances larger than 60 km, which is approximately the distance of the fault to the edge of the Reelfoot rift (RFR).

For the M_w 7.0 scenarios, the behavior between the simulated PGA and the GMPE is similar to the scenarios discussed above. In addition, the PGV and SA attenuation predicted by URSUSGSP and USGSG has different characteristics within 20 km. The latter predicts higher values for PGV and SA ($T = 2$ s) near the fault, but the amplitude decays faster with distance than the former. Again, the discrepancy could be due to the difference between the minimum velocities used in the simulations and frequency content of the source. The changes in attenuation slope are nearly consistent with the beginning of the transition zone (70–140 km) used in the GMPEs of the region for both magnitudes discussed (e.g., Atkinson and Boore, 2006; Pezeshk *et al.*, 2011). Notably, simulations reveal that the distances where the geometrical spreading factor exponent changes in GMPEs may be uncertain and/or variable.

In general, even though modelers used different techniques to generate the source rupture and minimum velocities, the ground motion in all cases is affected by the presence of the RFR, the boundary of which is displayed with a thick line in Figure 10, and rupture directivity. The effect of the RFR structure is seen in the synthetic ground-motion velocities and their Fourier amplitude spectra (Fig. 11), normalized by the maximum Fourier amplitude in the 0.0–1.0 Hz band, for the USGSG southern segment simulation (unilateral rupture M_w 7.7) along cross-section A–A′ (Fig. 10c). Data along cross-section A–A′ sample the ground-motion velocities crossing the fault near the epicenter and the boundaries of the RFR, thereby avoiding strong directivity effects and revealing the influence of the rift. Most of the energy trapped and propagating within the RFR is distributed in the ~0.1–0.4 Hz frequency band. In addition to the amplification and energy trapping by the RFR, strong rupture directivity is present (e.g., Somerville *et al.*, 1997), focusing energy to the southwest and northeast within the model. The di-

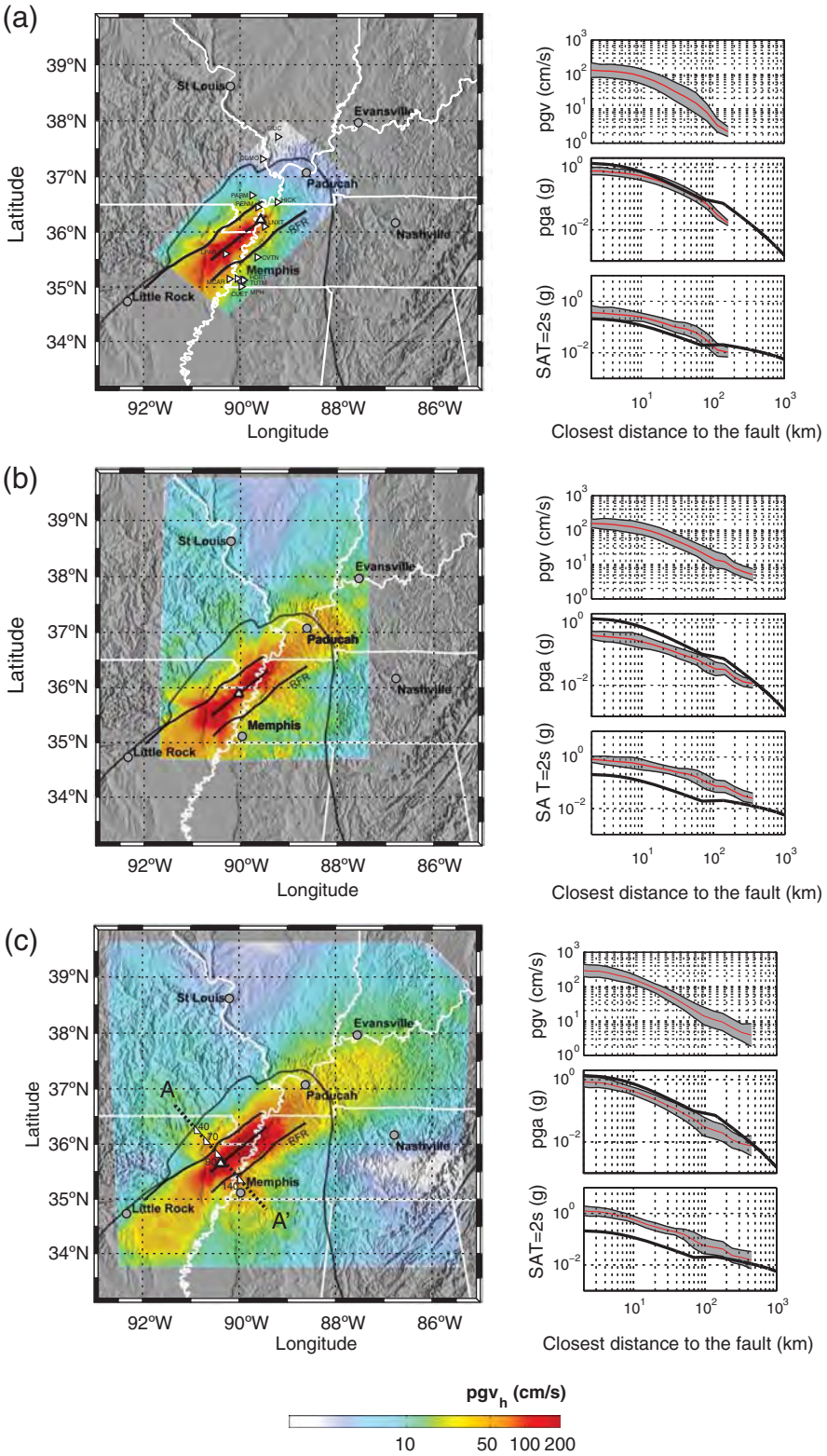

Figure 10. Ground-motion variability for NM1 events. Peak ground velocity (PGV) within the region simulated by each group, together with plots of PGV, peak ground acceleration (PGA), and spectral acceleration (SA) ($T = 2$ s) as a function of distance to the fault. The black continuous line indicates the PGA and SA computed using Pezeshk *et al.* (2011). (a) URSUSGSP simulation for an M_w 7.7 event in the southern segment: the trace of the fault is displayed as a thick black continuous line, with the hypocenter indicated by an upward-facing triangle. (b) Similar to (a) but with a different hypocenter for SDSU. (c) Similar to (a) but with a different hypocenter for USGSG. (d) Similar to (a) but with a different hypocenter for an M_w 7.0 event for URSUSGSP. (e) Similar to (d) but with a different hypocenter for USGSG. In (a), right-facing triangles are the locations of selected stations from Figure 11. In (c), the location of a linear array of stations is indicated with a discontinuous line. Left-facing triangles are selected reference stations (40, 70, 90, and 140) discussed in Figure 11. (*Continued*)

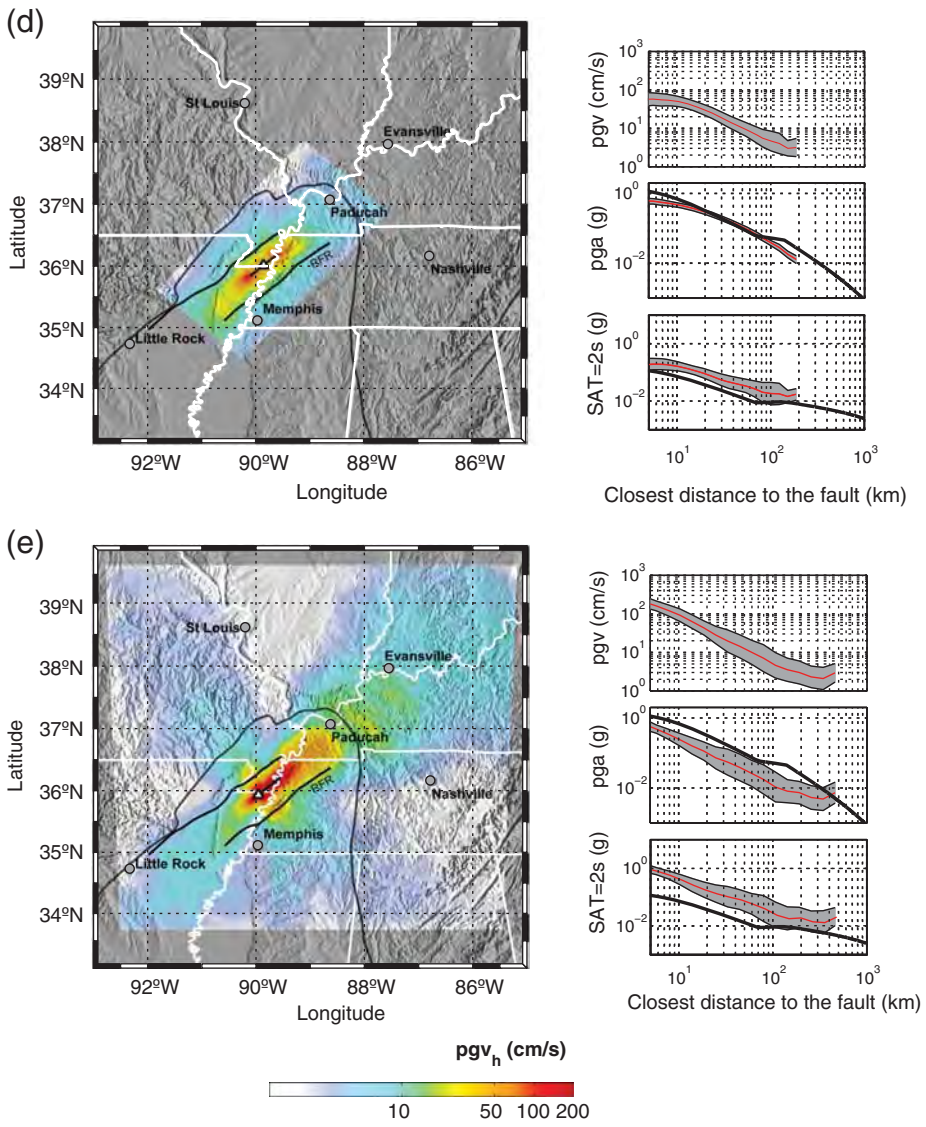

Figure 10. Continued.

rectivity is illustrated in Figure 12 for the URSUSGSP M_w 7.7 rupture that nucleated at the northwestern end of the southern segment; station locations are displayed in Figure 10a. Station LPAR, located in the forward (southwest) direction, shows the characteristic long-period (5 s) pulse due to the cumulative effect of the radiation from the fault. In contrast, station HICK in the backward (northeast) directivity region has very low amplitude and no clear dominant frequency.

The variability of the ground-motion velocity histories in the region is fairly large among all scenarios and stations. For instance, the 3–4 s surface waves in the Memphis (MPH, MCAR, and TUMT) region contrast with the almost imperceptible ground-motion velocities outside of the embayment (SIUC and CGMO). In our simulations, the ground motion in the St. Louis region is lower by factors from 5 to 10 than computed values in the forward (northeast or southwest, depending on the epicenter) direction of the rupture, where Paducah, Kentucky, Evansville, Indiana, and Little Rock, Arkansas, are located. Memphis, Tennessee, situated about 100 km southeast of the fault trace, exhibits PGV values between ~10 and ~50 cm/s, depending on the scenario, which are comparable to those seen in the regions subjected to directivity effects. Therefore, low ground motion in St. Louis does not mean lower-magnitude earthquakes in 1811–1812. Moreover, the strong ground motion phase (computed as the time to reach from 5% to 75% of the cumulative energy) around the Memphis metropolitan area could last from 30 to more than 60 s, which could potentially induce nonlinear incursions of the built structures.

Central Segment Rupture Simulations: Reelfoot Fault (NM3). Horizontal-velocity peak value maps, attenuation, and time histories for selected stations from four simulations in the central segment are displayed in Figures 13 and 14, in a similar fashion to Figures 10 and 12 for the southern segment

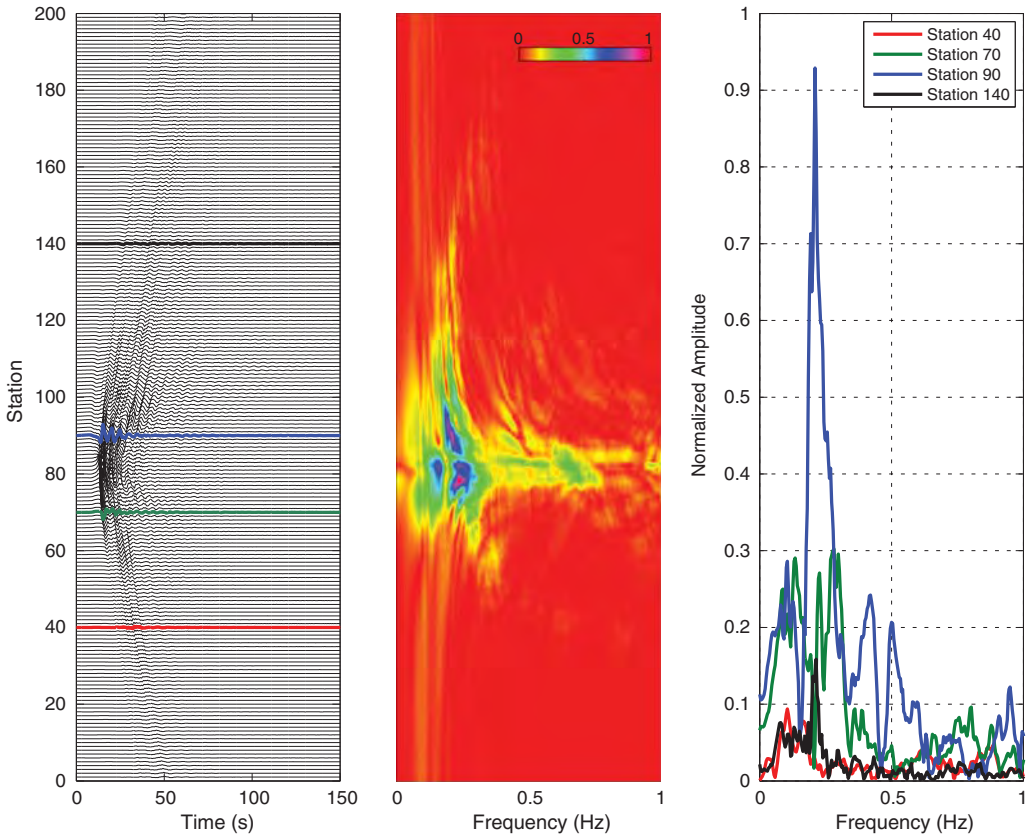

Figure 11. Ground velocities for the A–A′ cross section in Figure 10c. The time domain and Fourier amplitude normalized to the peak value are displayed. Stations 40, 70, 90, and 140 (identified with red, green, blue, and black continuous lines in the left panel, respectively) are displayed in the frequency domain in the right panel.

(see Ⓔ electronic supplement for the entire set). The ground-motion parameters are displayed for earthquakes with magnitudes 7.6 and 7.0. When compared with Pezeshk *et al.* (2011), the PGA trends share the same features discussed earlier; that is, the ratios between simulations and the GMPE remain within the same range, and PGA attenuation in the simulations declines more gradually than the values computed using the GMPE. In these simulations, the RFR does not act—or at least is not recognized—as a clear waveguide, as was observed in the southern segment simulations. In the M_w 7.6 and 7.0 simulations, large PGV (>50 cm/s) are mostly confined to distances within 40 and 20 km from the fault, respectively. Nevertheless, directivity effects prevail, especially for the M_w 7.6 earthquakes. Figure 14 illustrates the velocities at LNXT with a clear directivity pulse and the low ground motions at PARM, which is located in the backward (northwest) directivity region.

For the low-magnitude cases (M_w 7.0), we observe that the initial ground-motion decreasing trend changes, with few exceptions, from ~70 to ~100 km. These similarities with the proposed GMPEs for the region, together with the observations made, indicate consistency and potential validation of ground-motion characterization between our simulations and previous work but also reveal a strong dependency of the source location with the resulting ground motion.

Mean Intensities and Population Exposure

In terms of emergency manager planning and qualitative risk assessment, it is more important to have estimates of macroseismic intensity (such as the MMI) than predictions of ground-motion parameters like the ones computed in previous sections. By taking advantage of our simulations and previously developed correlations between ground-motion parameters and MMI, we estimated the size of the population exposed to various levels of intensity. Moreover, we used MMI and a distance–intensity attenuation model to show that, at least in the intermediate/far field, our simulation exercise is consistent with previous research.

The GMICEs of Atkinson and Kaka (2007) and Dangkua and Cramer (2011) provide a way to estimate the intensity when given a ground-motion parameter (PGA, PGV, or SA). As mentioned earlier, the bandwidth of the simulations was not uniform, except below 1.0 Hz. Only URSUSGSP generated full sets with 0–40 Hz bandwidth in a dense grid on the surface of the domain computed. Thus, the correlations between MMI and peak values of velocity (the ideal candidate for converting to MMI) and acceleration are inadequate for all simulations. Therefore, we used the correlations for the geometric mean of the SA ($T = 2$ s), which appropriately covers the bandwidth of all simulated records in the low-frequency range. We computed the intensities per simulation for the two magnitudes in the case of the southern and central segments.

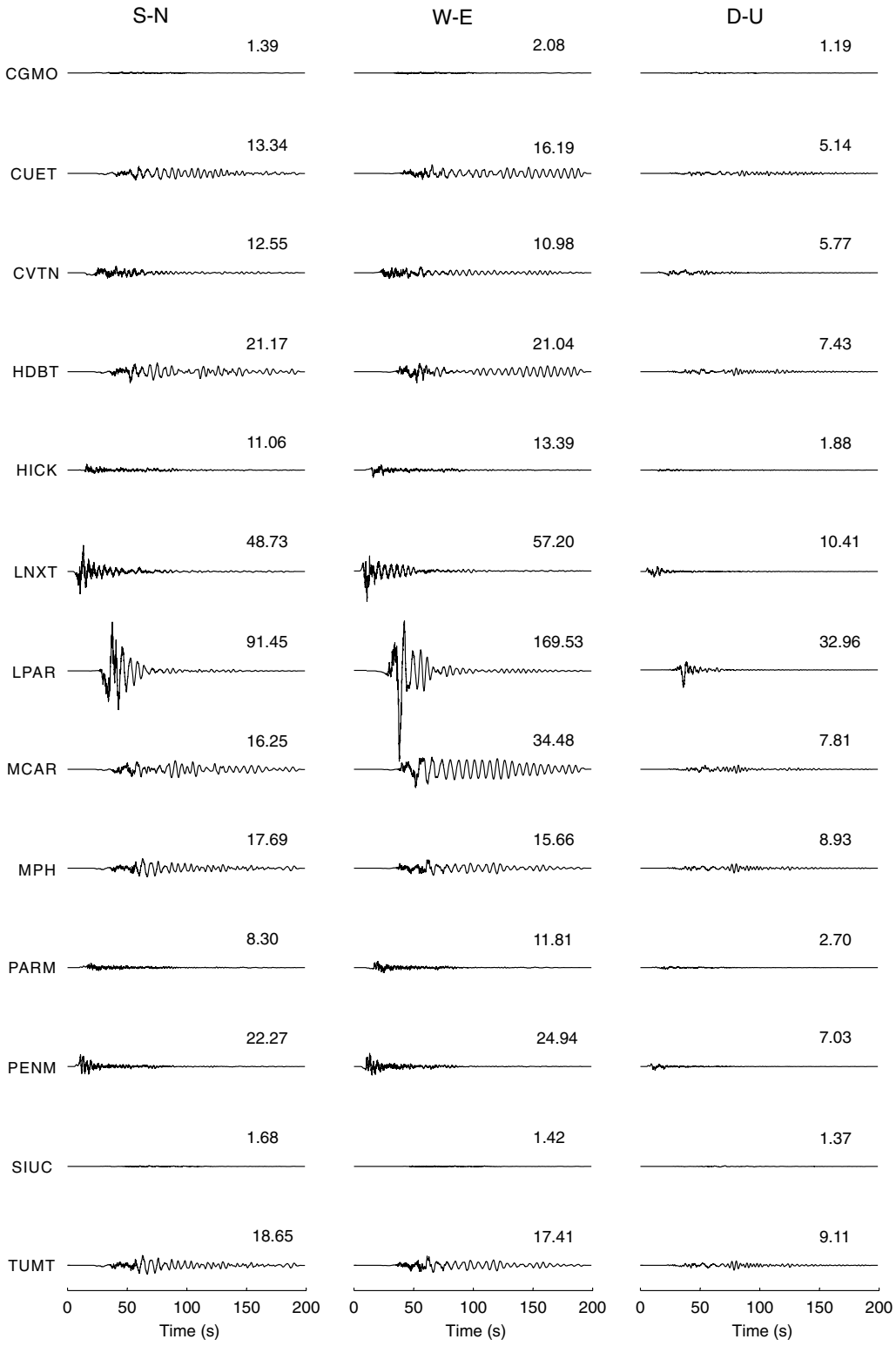

Figure 12. Broadband ground-motion velocities at selected stations for the M_w 7.7 simulation displayed in Figure 10a. Station LPAR, located in the forward (southwest) direction, shows the characteristic long-period pulse due to the cumulative effect of the radiation from the fault. Peak values are displayed for each signal. (S-N, south–north; W-E, west–east; D-U, vertical component.)

Figure 15 displays the mean intensity (plus one-half the standard deviation calculated using 30 bins in 590 km) as a function of distance compared against the Bakun and Hopper (2004) model 3 IPE (henceforth BH3) for **M** 7.0 and 7.7. This is the preferred intensity attenuation relation among the ones proposed by Bakun and Hopper (2004). The comparison

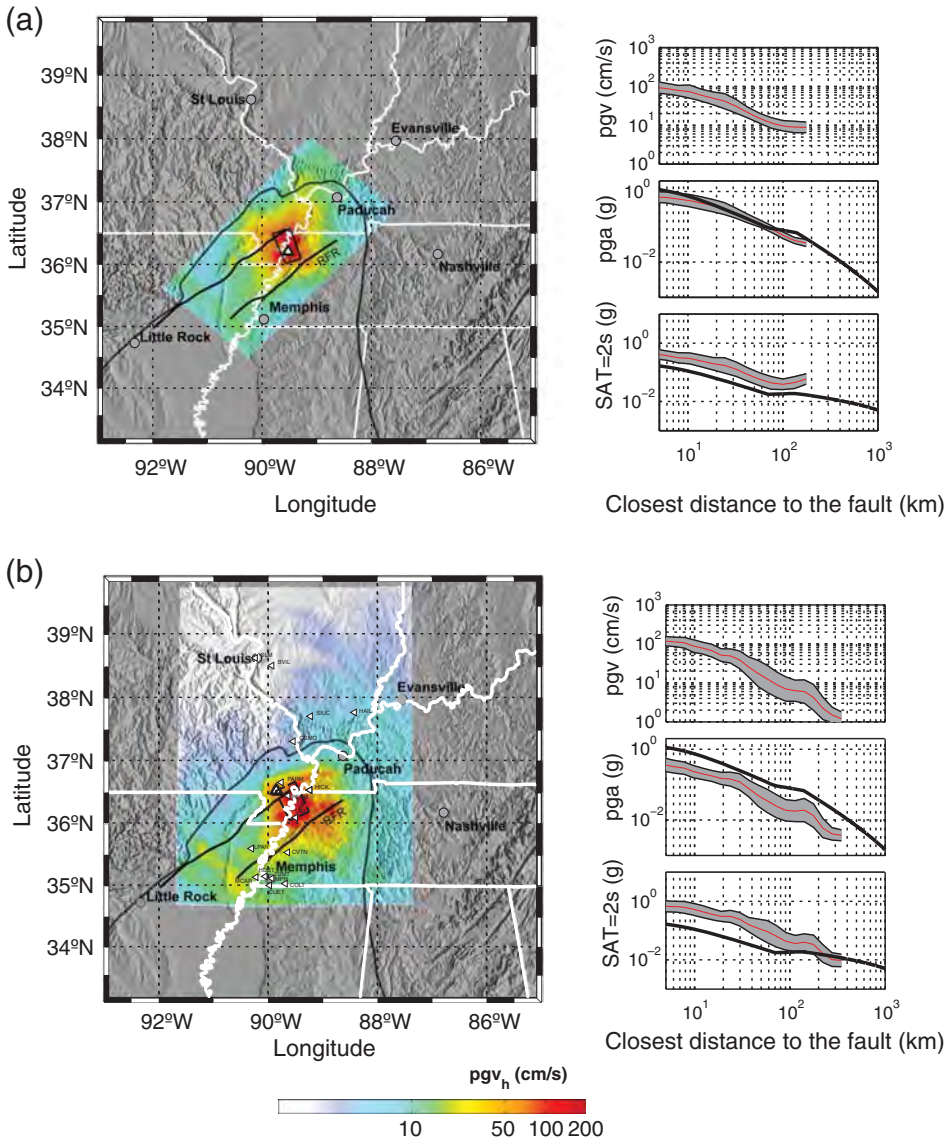

Figure 13. Ground-motion variability for NM3 events. Peak ground velocity within the region simulated by each group, together with plots of PGV, PGA, and SA ($T = 2$ s) as a function of distance from the fault. The black continuous line indicates the PGA and SA computed using Pezeshk *et al.* (2011). (a) URSUSGSP simulation for an M_w 7.6 simulation in the central segment: the trace of the fault is displayed as a thick black continuous line, with the hypocenter indicated by a triangle. (b) Similar to (a) but with a different hypocenter for SDSU. (C) URSUSGSP for an M_w 7.0 simulation. (d) USGSG for an M_w 7.0 simulation. (*Continued*)

reveals that the mean intensities in the near-source field predicted by the simulations are one to two units below the BH3 model. In the intermediate/far field, the same model is similar to the mean of the intensities for **M** 7.7 using Dangkua and Cramer (2011). In most cases, Atkinson and Kaka (2007) predict lower values than Dangkua and Cramer (2011) and are well under the BH3 model. We chose to use Dangkua and Cramer (2011) for the rest of this investigation because it is more consistent with our simulations. Figure 15b displays the same calculation for the NM3 scenarios. In that case, the intermediate/far field shows a better correlation than in the previous case, reinforcing our choice.

We calculated the population exposure relative to MMI for both magnitudes in the NM1 (M_w 7.0 and 7.7) and NM3 (M_w 7.0 and 7.6) scenarios using the mean intensity of all simulations at a cell size of ~1 km^2 (Fig. 16). We noted that practically the entire population (~16 million people) living within the limits of the largest region modeled (see Fig. 10c) would feel the earthquakes, whether M_w 7.0, 7.6, or 7.7. But more importantly, about 4 million and 2.5 million more people would be exposed to high intensities (damaging ground motions; VII and VIII) in the case of the high-magnitude earthquakes for NM1 and NM3 type scenarios, respectively. Thus, this exercise shows the importance of having a good estimate of the upper magnitude range of those earthquakes. Accordingly, in the following section and based on intensity estimates from our simulations, we explore the magnitudes of the December 1811 and February 1812 earthquakes. This preliminary

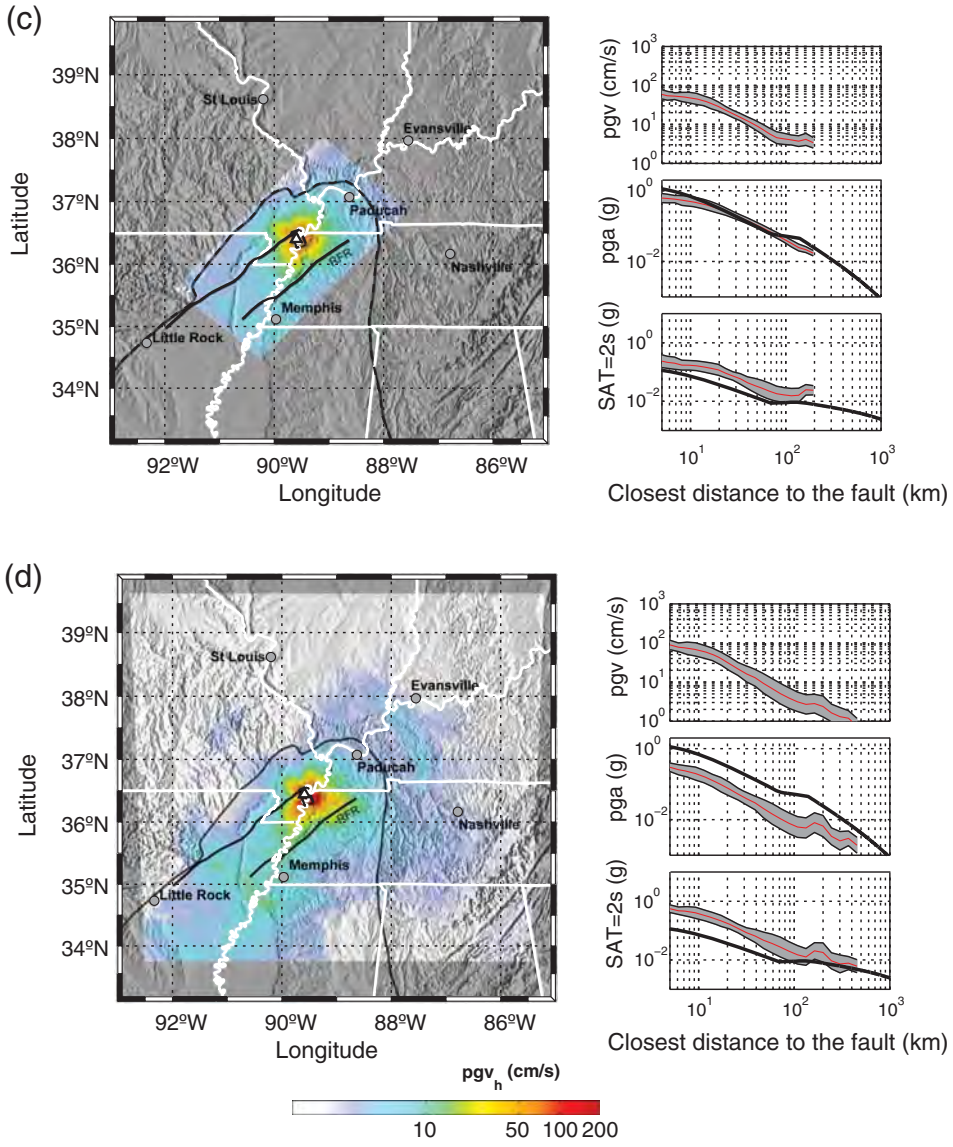

Figure 13. Continued.

exercise can lead us to some of the bounds and reveal some of the uncertainties involved in magnitude estimation procedures.

M_w Estimation

Establishing likely magnitudes for the historic events covered here is beyond the scope of this research. Nevertheless, we can evaluate the consistency of the obtained intensities for each of the simulated magnitudes with the historic MMI reports and suggest M_w estimates. Thus, we propose the following methodology:

1. Compute the mean of the MMI over the entire model area from the realizations—our set of simulations for each **M** (7.0, 7.7 and 7.0, 7.6)—using Dangkua and Cramer (2011) GMICE for the geometric mean of the SA ($T = 2$ s).
2. Compute the relative difference between the mean of the simulated MMIs with the reported MMI values. We use the reported MMI of Bakun *et al.* (2003) and the mean of the intensity assignments from Hough and Page (2011) within the modeled area.
3. Based on the mean and standard deviation of the relative difference between observed and computed intensities for each magnitude, we provide a preliminary magnitude.

These steps provide a crude estimate of the magnitude using only two sets of simulations with different magnitudes by comparing the means plus/minus standard deviations. A more robust approach would require an extensive database of probable scenarios with a full range of magnitudes, which could be analyzed to determine the most probable magnitude.

We use two sets of MMI reports, from Bakun *et al.* (2003) and Hough and Page (2011), to highlight the different results related to the probable subjectivity involved in the interpretation

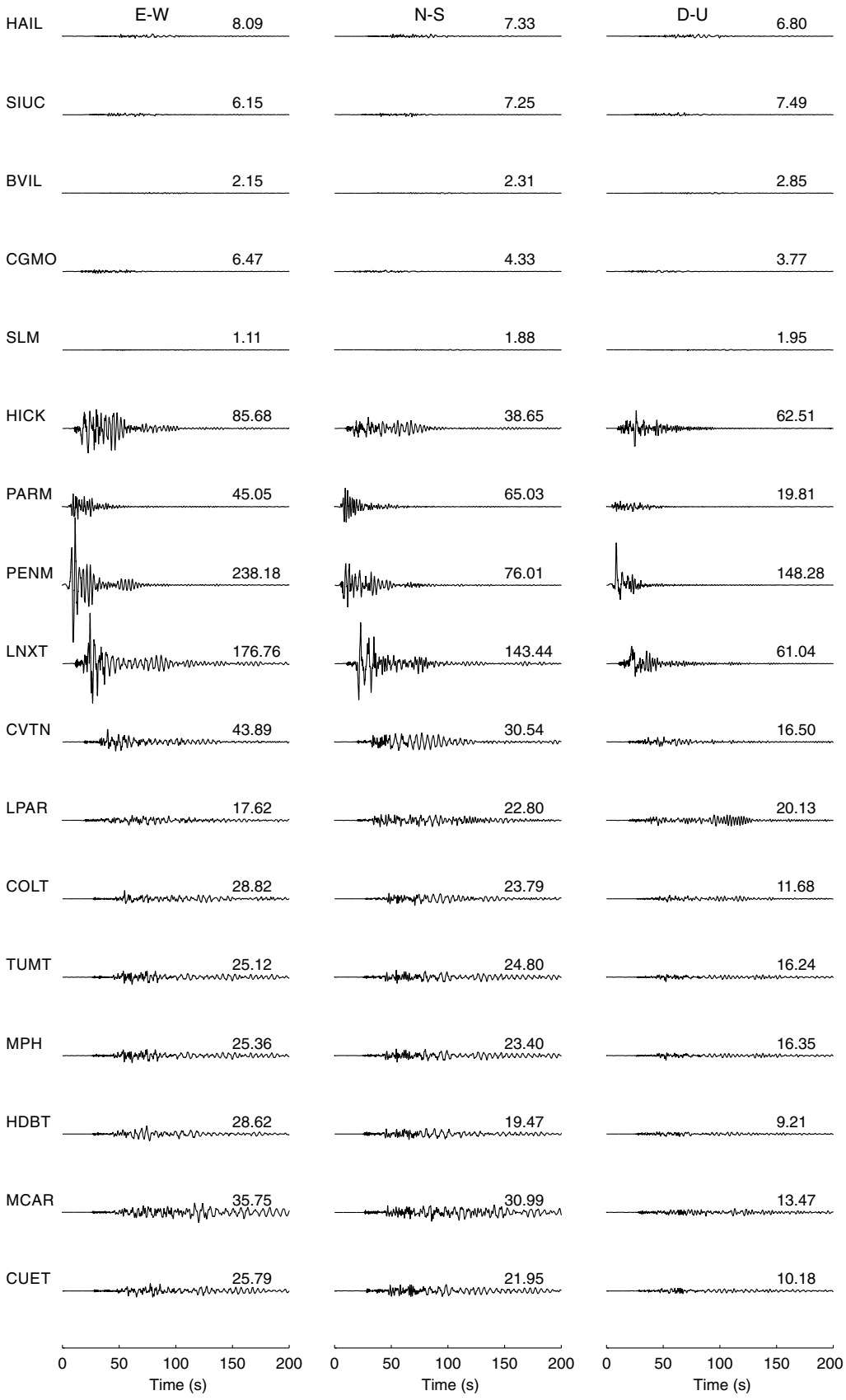

Figure 14. Broadband ground-motion velocities at selected stations for the simulation displayed in Figure 13b. Peak values are displayed for each signal. (S-N, south–north; W-E, west–east; D-U, vertical component.)

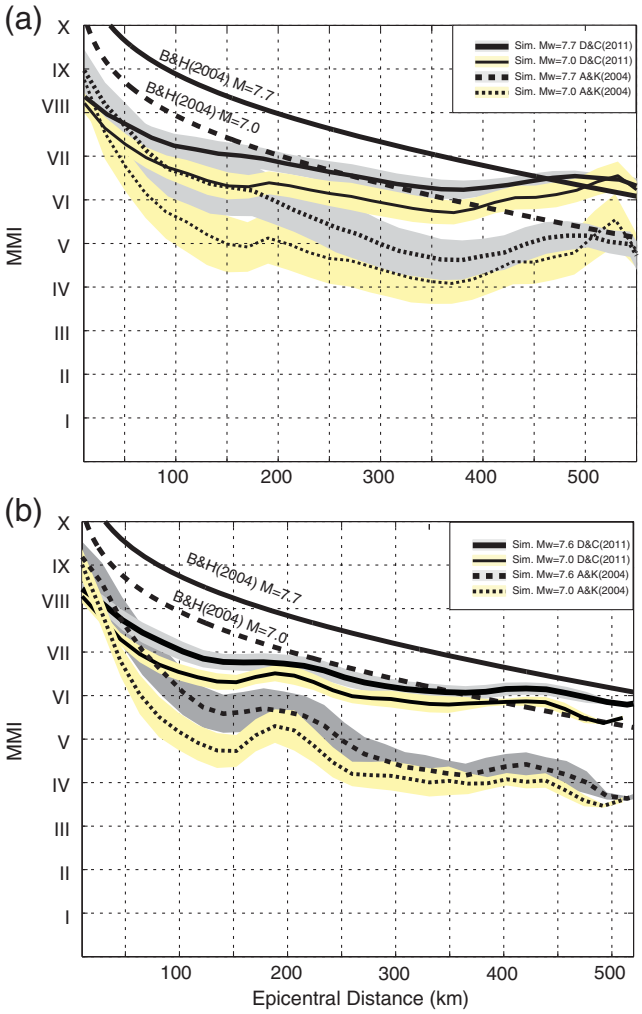

Figure 15. Modified Mercalli intensity (MMI) attenuation for (a) NM1 and (b) NM3. Intensity–distance computed with the ground-motion simulation's geometric mean of the SA ($T = 2$ s) using the Dangkua and Cramer (2011; continuous lines identified as D&C) and Atkinson and Kaka (2007; dashed lines identified as A&K). Ground-motion intensity correlation equations (GMICEs) compared with Bakun and Hopper (2004; identified as B&H) model 3 (thick continuous lines and dashed lines). The thick lines indicate high magnitude (7.7 and 7.6 for NM1 and NM3, respectively), and the thin lines show magnitude 7.0 based estimates. One standard deviation is displayed for each case based on simulations and GMICEs.

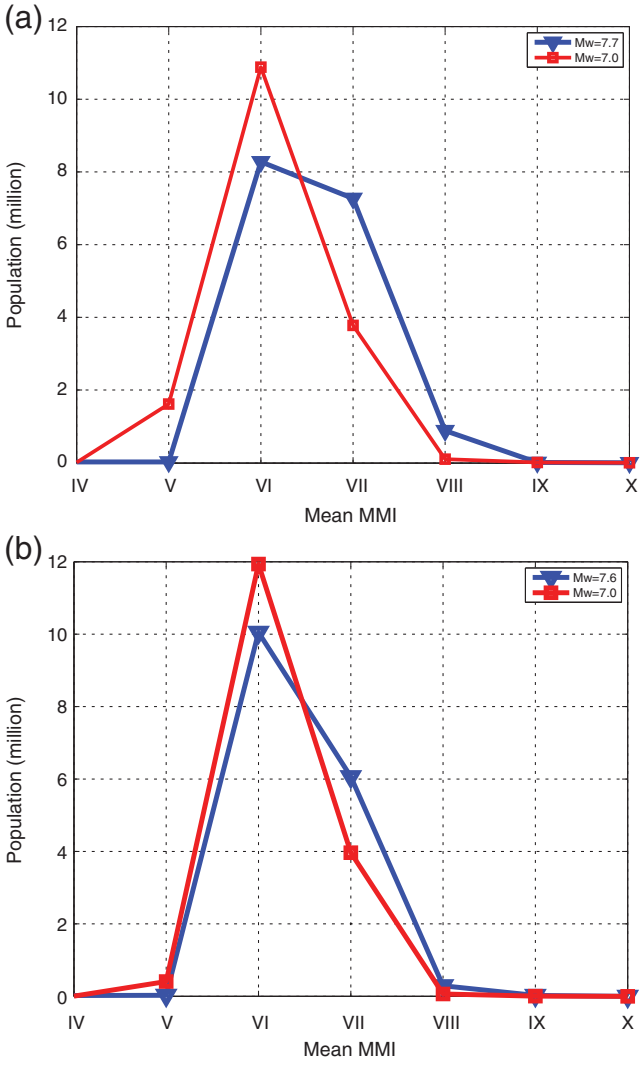

Figure 16. Population exposed to different levels of MMI according to the ground-motion simulation means of SA at $T = 2$ s and the Dangkua and Cramer (2011) GMICE. (a) The NM1 event with M_w 7.7 is in blue and M_w 7.0 is in red. (b) Same as (a) but for NM3 event (high M_w 7.6).

of historical accounts. As we mentioned earlier, Bakun and Hopper (2004) intended to use a consistent procedure to determine magnitude, using the same MMI interpretation subjectivity for the calibration events to derive the distance–intensity attenuation relationship and the historic events. Hough and Page (2011) used attenuation relations derived independently from the intensity assignments developed by four experts. In any case, the subjectivity involved is not ideal for magnitude calculations.

The normalized difference between predicted and observed intensity estimates for scenarios NM1 and NM3 is shown in Figure 17. When using Bakun *et al.* (2003), the simulations tend to underestimate the intensities for both the **M** 7.0 and 7.7 cases (see Fig. 17b and 17d), especially for the central segment rupture. This could in part be due to unmodeled low *S*-wave velocities (~180–300 m/s in the upper 30 m) known to exist in the region considered, which could induce either nonlinear effects and damping of ground-motion amplitudes and intensity or greater amplification of ground motions and intensity. In fact, widespread liquefaction was reported along with other ground failure (i.e., nonlinear effects) in the near-field historical accounts. The large magnitude scenarios, M_w 7.7 and 7.6 for NM1 and NM3, respectively, have a smaller mean relative difference between predicted and observed intensity, which in the absence of any other criteria would favor the large magnitudes. In contrast, when using Hough and Page (2011) intensity reports, we see an entirely different picture. In NM1 and NM3, the simulated intensities are much higher than Hough and Page (2011), and the low magnitudes have a lower mean difference between predicted and observed intensity. The lower magnitudes are consistent with their magnitude estimation. Thus, a key element in

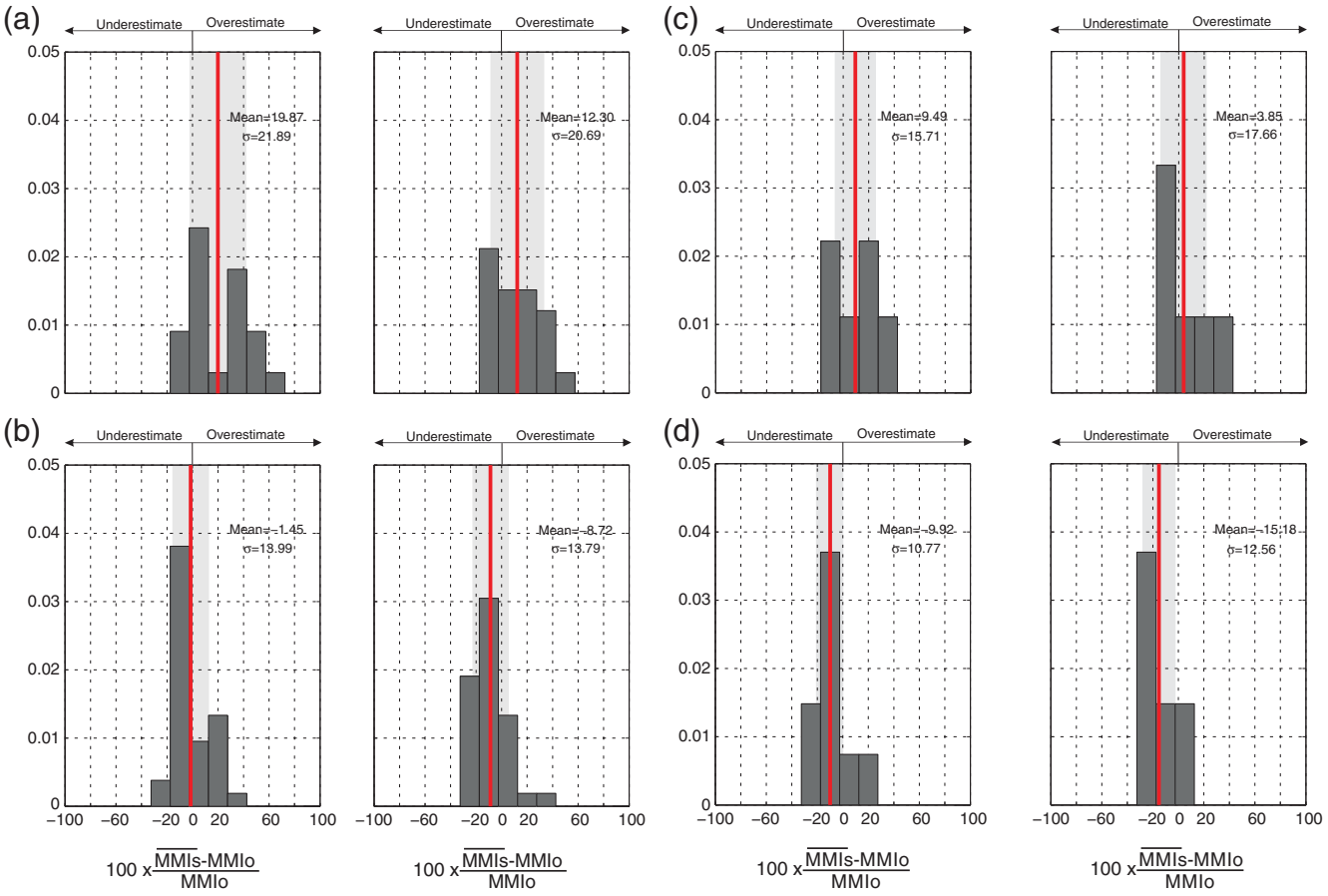

Figure 17. Relative difference distributions between the mean of the simulated MMIs with the reported MMI values for (left) high magnitude (M_w 7.7 for NM1 and 7.6 for NM3) and (right) low magnitude (M_w 7.0). (a,c) Relative difference distributions between the mean of the simulated MMIs (MMI_s) with the reported MMI values (MMI_o; using the Hough and Page, 2011, intensity assignments) and predicted MMI (using the mean simulated values of SA at $T = 2$ s and Dangkua and Cramer, 2011). (b,d) Same as (a) and (c) but using Bakun *et al.* (2003).

using ground-motion simulations to determine the size of the 1811–1812 sequence requires careful and consistent evaluation of the IPEs, GMICEs, and the intensity reports themselves.

Conclusions

A set of numerical simulations of NMSZ earthquakes (**M** 7.0–7.7) was performed to explore the variability and level of ground motion for possible large earthquakes in the CUS. Our simulations reveal strong basin and rupture directivity effects and long-duration shaking in the Mississippi embayment, especially for strike-slip earthquakes taking place along the Cottonwood Grove fault. These effects have not been widely considered in previous studies of the 1811–1812 events, and they add an additional level of uncertainty to attempt to constrain the magnitudes of these earthquakes.

Our simulated magnitude estimates for the NM1 and NM3 earthquakes at 7.7 and 7.6, respectively, produce calculated intensities similar to those used by Bakun and Hopper (2004). However, the uncertainty in constraining various aspects of the simulations and the subjectivity involved in assigning intensities to historical reports of shaking (which is not discussed here) does not rule out magnitudes as low as 7.0 for these events, such as proposed by Hough and Page (2011). For example, our simulations for an **M** 7.0 rupture starting at the western end of the Cottonwood Grove fault can produce stronger intensities toward the northeast (where most of the historical intensity observations are located) compared with that simulated for an **M** 7.7 rupture that starts at the eastern end of this fault. Thus, the ambiguity associated with epicentral location can translate directly into uncertainty in magnitude estimates, given the limited set of intensity observations.

Nonetheless, even at the lower-magnitude threshold considered in our simulations (**M** 7.0), strong shaking is predicted over a very large region, with several million people likely experiencing MMI V or higher intensities in each scenario. In addition, for the higher-magnitude scenarios (**M** 7.6 and 7.7), up to 4 million people could be exposed to intensity MMI VII or higher. Thus, it is important to have a good estimate of the upper magnitude range of potential earthquakes available and to determine the likelihood of a sequence similar to the one described in this research.

Data and Resources

The Central United States Velocity Model v.1.2 and v.1.3 are available upon request and at http://earthquake.usgs.gov/

research/cus_seisvelmodel/ (last accessed August 2014). The ground-motion data mentioned in the Appendix and used in the Ⓔ electronic supplement were obtained from the St. Louis University (http://www.eas.slu.edu/eqc/eqc_events/2008EQ.DATA/index.html; last accessed November 2014) and Incorporated Research Institutions for Seismology (IRIS; http://www.iris.edu/hq/, last accessed November 2014) websites. U.S. Geological Survey Golden (USGSG) computations were performed on Kraken at the National Institute for Computational Sciences (http://www.nics.tennessee.edu/; last accessed September 2012).

Acknowledgments

This research was supported by the TG-EAR090003 allocation for advanced computing resources provided by the National Science Foundation. Michael Hearn at the U.S. Geological Survey (USGS) National Earthquake Information Center (NEIC) provided the script to compute the exposed population. Several aspects of this work were performed by L.R.-G. during his time as a postdoctoral research contractor at the USGS-Golden office. Part of the work by L.R.-G. was financed by the Instituto de Ingeniería at Universidad Nacional Autónoma de México. We thank Jer-Ming Chiu, Steve Horton, Charles Langston, and Christine Powell at the Center for Earthquake Research and Information (CERI) and Walter Mooney at the USGS Menlo Park office for the expert opinions they provided in several conversations. We thank Christina Boyes for her assistance in the editing and proofreading of this manuscript. We thank Susan Hough and two anonymous reviewers whose comments and critiques improved the manuscript. This research was supported in part by the USGS Earthquake Hazards Program Grants G10AP00007 and G09AP00139. Any use of trade, product, or firm names is for descriptive purposes only and does not imply endorsement by the U.S. Government or any institution mentioned.

References

Aagaard, B., T. Brocher, D. Dolenc, D. Dreger, R.W. Graves, S. Harmsen, S. Hartzell, S. Larsen, and M. Zoback (2008a). Ground-motion modeling of the 1906 San Francisco earthquake, Part I: Validation using the 1989 Loma Prieta earthquake, *Bull. Seismol. Soc. Am.* **98,** 989–1011.

Aagaard, B., T. Brocher, D. Dolenc, D. Dreger, R. W. Graves, S. Harmsen, S. Hartzell, S. Larsen, K. McCandless, S. Nilsson, *et al.* (2008b). Ground-motion modeling of the 1906 San Francisco earthquake, Part II, Ground-motion estimates for the 1906 earthquake and scenario events, *Bull. Seismol. Soc. Am.* **98,** 1012–1046.

Andrews, M. C., W. D. Mooney, and R. P. Meyer (1985). Relocation of microearthquakes from the northern Mississippi embayment, *J. Geophys. Res.* **90,** no. B12, 10,223–10,236.

Atkinson, G. M., and D. M. Boore (1995). Ground-motion relations for eastern North America, *Bull. Seismol. Soc. Am.* **85,** no. 1, 17–30.

Atkinson, G. M., and D. M. Boore (2006). Earthquake ground-motion prediction equations for eastern North America, *Bull. Seismol. Soc. Am.* **96,** no. 6, 2181–2205.

Atkinson, G. M., and D. M. Boore (2011). Modifications to existing ground-motion prediction equations in light of new data, *Bull. Seismol. Soc. Am.* **101,** no. 3, 1121–1135.

Atkinson, G. M., and S. L. Kaka (2007). Relationships between felt intensity and instrumental ground motion in the central United States and California, *Bull. Seismol. Soc. Am.* **97,** no. 2, 497–510.

Atkinson, G. M., and D. J. Wald (2007). "Did You Feel It?" intensity data: A surprisingly good measure of earthquake ground motion, *Seismol. Res. Lett.* **78,** 362–368.

Bakun, W. H., and M. G. Hopper (2004). Magnitudes and locations of the 1811–1812 New Madrid, Missouri, and the 1886 Charleston, South Carolina, earthquake, *Bull. Seismol. Soc. Am.* **94,** no. 1, 64–75.

Bakun, W. H., and C. M. Wentworth (1997). Estimating earthquake location and magnitude from seismic intensity data, *Bull. Seismol. Soc. Am.* **87,** no. 6, 1502–1521.

Bakun, W. H., A. C. Johnston, and M. G. Hopper (2002). Modified Mercalli intensities (MMI) for large earthquakes near New Madrid, Missouri, in 1811–1812 and near Charleston, South Carolina, in 1886, *U.S. Geol. Surv. Open-File Rept. 02-184*, 31 pp.

Bakun, W. H., A. C. Johnston, and M. G. Hopper (2003). Estimating locations and magnitudes of earthquakes in eastern North America from modified Mercalli intensities, *Bull. Seismol. Soc. Am.* **93,** no. 1, 190–202.

Baldwin, J. N., J. B. Harris, R. B. Van Arsdale, R. Givler, K. I. Kelson, J. L. Sexton, and M. Lake (2005). Constraints on the location of the Late Quaternary Reelfoot and New Madrid North faults in the northern New Madrid seismic zone, central United States, *Seismol. Res. Lett.* **76,** 772–789.

Bielak, J., R. W. Graves, K. B. Olsen, R. Taborda, L. Ramirez-Guzman, S. M. Day, G. P. Ely, D. Roten, T. H. Jordan, P. J. Maechling, *et al.* (2010). The ShakeOut earthquake scenario: Verification of three simulation sets, *Geophys. J. Int.* **180,** 375–404.

Bodin, P., and S. Horton (1999). Broadband microtremor observations of basin resonance in the Mississippi embayment, central U.S., *Geophys. Res. Lett.* **26,** 903–906.

Boore, D. M. (1983). Stochastic simulation of high-frequency ground motions based on seismological models of the radiated spectra, *Bull. Seismol. Soc. Am.* **73,** no. 6, 1865–1894.

Boyd, O. S., and C. H. Cramer (2014). Estimating earthquake magnitudes from reported intensities in the central and eastern United States, *Bull. Seismol. Soc. Am.* **104,** no. 4, 1709–1722.

Calais, E., and S. Stein (2009). Time-variable deformation in the New Madrid seismic zone, *Science* **323,** 1442.

Calais, E., A. M. Freed, R. Van Arsdale, and S. Stein (2010). Triggering of New Madrid seismicity by late-Pleistocene erosion, *Nature* **466,** 608–612.

Campbell, K. W., and Y. Bozorgnia (2012). Cumulative absolute velocity (CAV) and seismic intensity based on the PEER-NGA database, *Earthq. Spectra* **28,** no. 2, 457–485.

Chen, H., J. M. Chiu, J. Pujol, K. Kim, K. C. Chen, B. S. Huang, Y. H. Yeh, and S. C. Chiu (2006). A simple algorithm for local earthquake location using 3D V_P and V_S models: Test examples in the central United States and in central eastern Taiwan, *Bull. Seismol. Soc. Am.* **96,** no. 1, 288–305.

Chiu, J. M., A. C. Johnston, and Y. T. Yang (1992). Imaging the active faults of the central New Madrid seismic zone using PANDA array data, *Seismol. Res. Lett.* **63,** no. 3, 375–393.

Cramer, C. H., and O. S. Boyd (2014). Why the New Madrid earthquakes are M7–8 and the Charleston earthquake is ∼M7, *Bull. Seismol. Soc. Am.* **104,** no. 6, 2884.

Csontos, R., and R. Van Arsdale (2008). New Madrid seismic zone fault geometry, *Geosphere* **4,** 802–813.

Dalguer, L. A., H. Miyake, S. M. Day, and K. Irikura (2008). Calibrated surface and buried dynamic rupture models constrained with statistical observations of past earthquakes, *Bull. Seismol. Soc. Am.* **98,** 1147–1161

Dangkua, D. T., and C. H. Cramer (2011). Felt intensity versus instrumental ground motion: A difference between California and eastern North America? *Bull. Seismol. Soc. Am.* **101,** no. 4, 1847–1858.

Dorman, J., and R. Smalley (1994). Low-frequency seismic surface waves in the upper Mississippi embayment, *Seismol. Res. Lett.* **65,** no. 2, 137–148.

Dunn, M., S. Horton, H. R. DeShon, and C. A. Powell (2010). High resolution earthquake location in the New Madrid seismic zone, *Seismol. Res. Lett.* **81,** 406–413.

Evernden, J. F. (1967). Magnitude determination at regional and near-regional distances in the United States, *Bull. Seismol. Soc. Am.* **57,** no. 4, 591–639.

Frankel, A., R. Smalley, and J. Paul (2012). Significant motions between GPS sites in the New Madrid region: Implications for seismic hazard, *Bull. Seismol. Soc. Am.* **102,** no. 2, 479–489.

Fuller, M. L. (1912). The New Madrid earthquake, *U.S. Geol. Surv. Bull. 494*, 199 pp.

Gomberg, J. S. (1992). Tectonic deformation in the New Madrid seismic zone: Inferences from boundary element modeling, *Seismol. Res. Lett.* **63,** no. 3, 407–425.

Goulet, C. A., N. A. Abrahamson, P. G. Somerville, and K. E. Wooddell (2015). The SCEC Broadband Platform Validation Exercise: Methodology for code validation in the context of seismic-hazard analyses, *Seismol. Res. Lett.* **86,** 17–26.

Graves, R. W. (1996). Simulating seismic wave propagation in 3D elastic media using staggered-grid finite differences, *Bull. Seismol. Soc. Am.* **86,** no. 4, 1091–1106.

Graves, R. W., and A. Pitarka (2010). Broadband ground-motion simulation using a hybrid approach, *Bull. Seismol. Soc. Am.* **100,** no. 5A, 2095–2123.

Grollimund, B., and M. D. Zoback (2001). Did deglaciation trigger intraplate seismicity in the New Madrid seismic zone? *Geology* **29,** 175–178.

Hanks, T. C., and W. H. Bakun (2008). M-log A observations for recent large earthquakes, *Bull. Seismol. Soc. Am.* **98,** no. 1, 490–494.

Hartzell, S., and C. Mendoza (2011). Source and site response study of the 2008 Mount Carmel, Illinois, earthquake, *Bull. Seismol. Soc. Am.* **101,** 951–963.

Hough, S. E. (2004). Scientific overview and historical context of the 1811–1812 New Madrid earthquake sequence, *Ann. Geophys.* **47,** 523–537.

Hough, S. E. (2009). Cataloging the 1811–1812 New Madrid, central U.S. earthquake sequence, *Seismol. Res. Lett.* **80,** no. 6, 1045–1053.

Hough, S. E., and M. Page (2011). Toward a consistent model for strain accrual and release for the New Madrid seismic zone, central United States, *J. Geophys. Res.* **116,** no. B03311, doi: 10.1029/2010JB007783.

Hough, S. E., J. G. Armbruster, L. Seeber, and J. F. Hough (2000). On the modified Mercalli intensities and magnitudes of the 1811–1812 New Madrid earthquakes, *J. Geophys. Res.* **105,** no. B10, 23,839–23,864.

Johnston, A. C. (1996). Seismic moment assessment of earthquakes in stable continental regions—III, New Madrid 1811–1812, Charleston1886, and Lisbon 1755, *Geophys. J. Int.* **126,** 314–344.

Johnston, A. C., and E. S. Schweig (1996). The enigma of the New Madrid earthquakes of 1811–1812, *Annu. Rev. Earth Planet. Sci.* **24,** 339–384.

Kaka, S. I., and G. M. Atkinson (2004). Relationships between instrumental ground-motion parameters and modified Mercalli intensity in eastern North America, *Bull. Seismol. Soc. Am.* **94,** no. 5, 1728–1736.

Kanter, L. R. (1994). Tectonic interpretation of stable continental crust, in *The Earthquakes of Stable Continental Regions*, A. C. Johnston, K. J. Coppersmith, L. R. Kanter, and C. A. Cornell (Editors), Chapter 2, Vol. 1, Report for Electric Power Research Institute (EPRI), Palo Alto, California, EPRI TR 102261, 1–98.

Kenner, S., and P. Segall (2000). A mechanical model for intraplate earthquakes: Application to the New Madrid seismic zone, *Science* **289,** 2329–2332.

Langston, C. A., P. Bodin, C. Powell, M. Withers, S. Horton, and W. Mooney (2006). Explosion source strong ground motions in the Mississippi embayment, *Bull. Seismol. Soc. Am.* **96,** 1038–1054.

Leonard, M. (2010). Earthquake fault scaling: Self-consistent relating of rupture length, width, average displacement, and moment release, *Bull. Seismol. Soc. Am.* **100,** no. 5A, 1971–1988.

Liu, L., and M. D. Zoback (1997). Lithospheric strength and intraplate seismicity in the New Madrid seismic zone, *Tectonics* **16,** 585–595.

Liu, P., R. Archuleta, and S. H. Hartzell (2006). Prediction of broadband ground motion time histories: Frequency method with correlation random source parameters, *Bull. Seismol. Soc. Am.* **96,** 2118–2130.

Macpherson, K. A., E. W. Woolery, Z. Wang, and P. Liu (2010). Three-dimensional long-period ground-motion simulations in the upper Mississippi embayment, *Seismol. Res. Lett.* **8,** no. 2, 391–405.

Mai, P. M., and G. C. Beroza (2002). A spatial random field model to characterize complexity in earthquake slip, *J. Geophys. Res.* **107,** no. B11, 2308.

Mai, P. M., and G. C. Beroza (2003). A hybrid method for calculating near-source, broadband seismograms: Applications to strong motion prediction, *Phys. Earth. Planet In.* **137,** 183–199.

Mai, P. M., W. Imperatori, and K. B. Olsen (2010). Hybrid broadband ground motion simulations: Combining long-period deterministic synthetics with high-frequency multiple *S*-to-*S* backscattering, *Bull. Seismol. Soc. Am.* **100,** no. 5A, 2124–2142.

McKenna, J., S. Stein, and C. A. Stein (2007). Is the New Madrid seismic zone hotter and weaker than its surroundings? *Geol. Soc. Am. Spec. Pap.* **425,** 167–175.

Mena, B., P. M. Mai, K. B. Olsen, M. D. Purvance, and J. N. Brune (2010). Hybrid broadband ground-motion simulation using scattering Green's functions: Application to large-magnitude events, *Bull. Seismol. Soc. Am.* **100,** no. 5A, 2143–2162.

Motazedian, D., and G. M. Atkinson (2005). Stochastic finite-fault modeling based on a dynamic corner frequency, *Bull. Seismol. Soc. Am.* **95,** no. 3, 995–1010.

Nuttli, O. W. (1973a). Seismic wave attenuation and magnitude relations for eastern North America, *J. Geophys. Res.* **78,** no. 5, 876–885.

Nuttli, O. W. (1973b). The Mississippi Valley earthquakes of 1811 and 1812: Intensities, ground motion, and magnitudes, *Bull. Seismol. Soc. Am.* **63,** 227–248.

Olsen, K. B., and R. J. Archuleta (1996). Three-dimensional simulation of earthquakes on the Los Angeles fault system, *Bull. Seismol. Soc. Am.* **86,** no. 3, 575–596.

Olsen, K. B., and J. E. Mayhew (2010). Goodness-of-fit criteria for broadband synthetic seismograms, with application to the 2008 M_w 5.4 Chino Hills, CA, earthquake, *Seismol. Res. Lett.* **81,** 715–723.

Petersen, M. D., A. D. Frankel, S. C. Harmsen, C. S. Mueller, K. M. Haller, R. L. Wheeler, R. L. Wesson, Y. Zeng, O. S. Boyd, D. M. Perkins, *et al.* (2008). Documentation for the 2008 update of the United States National Seismic Hazard Maps, *U.S. Geol. Surv. Open-File Rept. 2008-1128*, 119 pp.

Petersen, M. D., M. P. Moschetti, P. M. Powers, C. S. Mueller, K. M. Haller, A. D. Frankel, Y. Zeng, S. Rezaeian, S. C. Harmsen, O. S. Boyd, *et al.* (2014). Documentation for the 2014 update of the United States National Seismic Hazard Maps, *U.S. Geol. Surv. Open-File Rept. 2014-1091*, 243 pp.

Pezeshk, S., A. Zandieh, and B. Tavakoli (2011). Hybrid empirical ground-motion prediction equations for eastern North America using NGA models and updated seismological parameters, *Bull. Seismol. Soc. Am.* **101,** no. 4, 1859–1870.

Pollitz, F. F., L. Kellogg, and R. Burgmann (2001). Sinking Mafic body in a reactivated lower crust: A mechanism for stress concentration at the New Madrid seismic zone, *Bull. Seismol. Soc. Am.* **91,** 1882–1897.

Ramirez-Guzman, L., O. S. Boyd, S. Hartzell, and R. A. Williams (2010). Earthquake ground motion simulations in the central United States, *AGU Fall Meeting 2010*, San Francisco, California, December 2010, Abstract S53D-06.

Ramírez-Guzmán, L., O. S. Boyd, S. Hartzell, and R. A. Williams (2012). Seismic velocity model of the central United States (Version 1): Description and simulation of the 18 April 2008 Mt. Carmel, Illinois, earthquake, *Bull. Seismol. Soc. Am.* **102,** no. 6, 2622–2645.

Riddell, R. (2007). On ground motion intensity indices, *Earthq. Spectra* **23,** no. 1, 147–173.

Saikia, C. K., A. Pitarka, and G. A. Ichinose (2006). Effects of irregular structure of the Mississippi embayment on ground-motion amplification, *Bull. Seismol. Soc. Am.* **96,** no. 4a, 1448–1473.

Shaw, B. E (2009). Constant stress drop from small to great earthquakes in magnitude-area scaling, *Bull. Seismol. Soc. Am.* **99,** no. 2A, 871–875.

Sipkin, S. A. (2003). A correction to body-wave magnitude m_b based on moment magnitude M_w, *Seismol. Res. Lett.* **74,** no. 6, 739–742.

Somerville, P., R. Graves, N. Collins, S. G. Song, S. Ni, and P. Cummins (2009). Source and ground motion models for Australian earthquakes, *Proc. 2009 Annual Conference of the Australian Earthquake Engineering Society*, Newcastle, New South Wales, December 2009, 11–13.

Somerville, P, K. Irikura, R. Graves, S. Sawada, D. Wald, N. Abrahamson, Y. Iwasaki, T. Kagawa, N. Smith, and A. Kowada (1999). Characterizing crustal earthquake slip models for the prediction of strong ground motion, *Seismol. Res. Lett.* **70,** no. 1, 59–80.

Somverville, P. G., N. F. Smith, R. W. Graves, and N. A. Abrahamson (1997). Modification of empirical strong ground motion attenuation relations to include the amplitude and duration effects of rupture directivity, *Seismol. Res. Lett.* **68,** no. 1, 199–222.

Stauder, W., M. Kramer, G. Fischer, S. Schaefer, and S. T. Morrissey (1976). Seismic characteristics of southeast Missouri as indicated by a regional telemetered microearthquake array, *Bull. Seismol. Soc. Am.* **66,** no. 6, 1953–1964.

Stephenson, W. J., J. K. Odum, R. A. Williams, T. L. Pratt, R. W. Harrison, and D. Hoffman (1999). Deformation and quaternary faulting in southeast Missouri across the Commerce geophysical lineament, *Bull. Seismol. Soc. Am.* **89,** 140–155.

Street, R., E. W. Woolery, Z. Wang, and J. B. Harris (2001). NEHRP soil classifications for estimating site-dependent seismic coefficients in the upper Mississippi embayment, *Eng. Geol.* **62,** 123–135.

Tu, T., H. Yu, L. Ramirez-Guzman, J. Bielak, O. Ghattas, K. L. Ma, and D. O'Hallaron (2006). From mesh generation to scientific visualization: An end-to-end approach to parallel supercomputing, *Proceedings of the 2006 ACM/IEEE Conference on Supercomputing*, Tampa, Florida, 11–17 November 2006.

Tuttle, M., E. S. Schweig, J. D. Sims, R. H. Lafferty, L. Wolf, and M. Haynes (2002). The earthquake potential of the New Madrid seismic zone, *Bull. Seismol. Soc. Am.* **92,** 2080–2089.

Van Arsdale, R. (2000). Displacement history and slip rate on the Reelfoot fault of the New Madrid seismic zone, *Eng. Geol.* **55,** 219–226.

Wells, D. L., and K. J. Coppersmith (1994). New empirical relationships among magnitude, rupture length, rupture width, rupture area, and surface displacement, *Bull. Seismol. Soc. Am.* **84,** no. 4, 974–1002.

Wood, H. O., and F. Neumann (1931). Modified Mercalli intensity scale of 1931, *Bull. Seismol. Soc. Am.* **21,** 277–283.

Yen, Y.-T., and K.-F. Ma (2011). Source-scaling relationship for M 4.6–8.9 earthquakes, specifically for earthquakes in the collision zone of Taiwan, *Bull. Seismol. Soc. Am.* **101,** no. 2, 464–481.

Zeng, Y. H., F. Su, and K. Aki (1991). Scattering wave energy propagation in a random isotropic scattering medium. 1. Theory, *J. Geophys. Res.* **96,** 607–619.

Zhu, L., and L. A. Rivera (2002). A note on the dynamic and static displacements from a point source in multilayered media, *Geophys. J. Int.* **148,** no. 3, 619–627.

Appendix

Code Verification

The three codes used in this research were verified by visual inspection and a variation of the goodness-of-fit (GOF) method proposed by Olsen and Mayhew (2010) using the 18 April 2008 M_w 5.4 Mount Carmel, Illinois, earthquake.

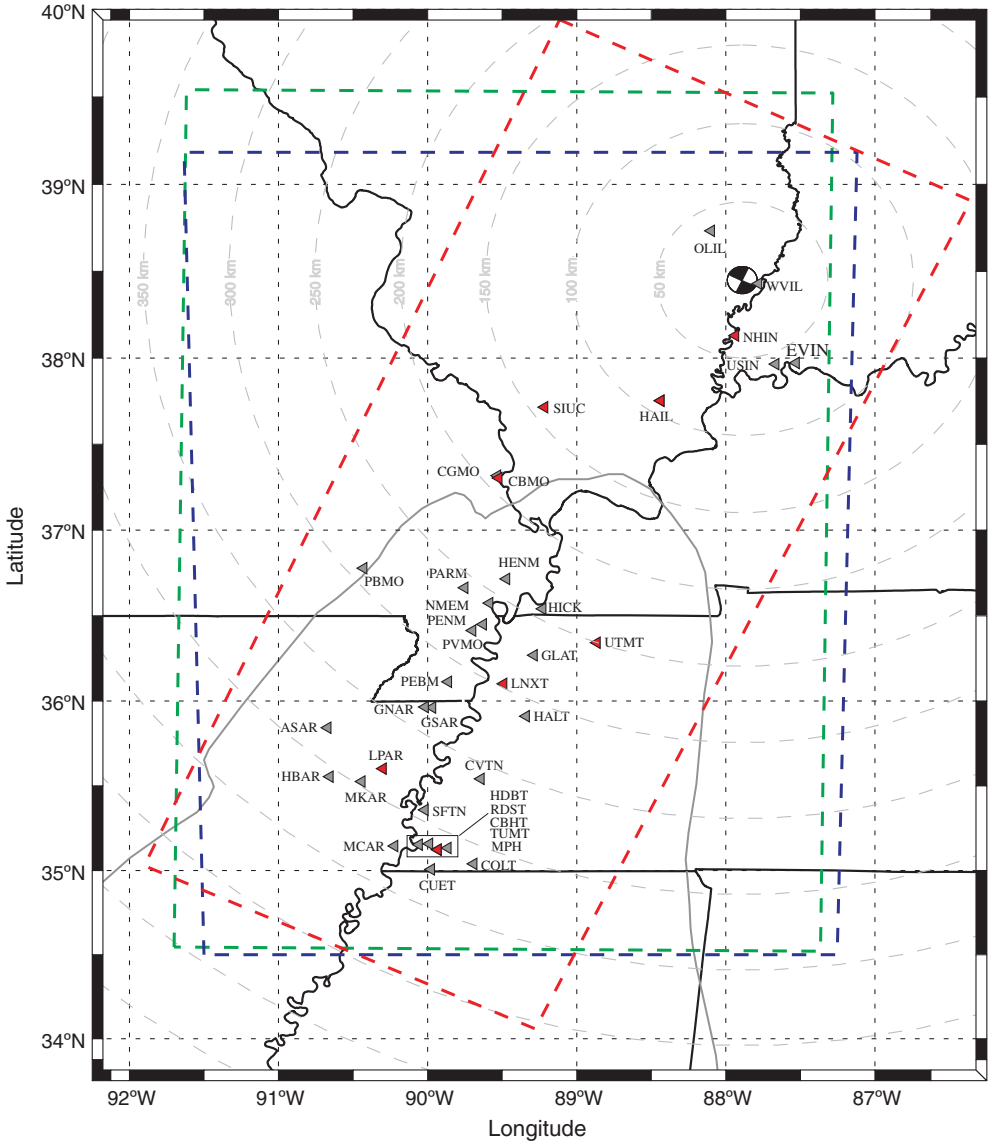

Figure A1. Simulation domains and stations considered in the verification. Red, blue, and green dashed quadrilaterals depict the UR-SUSGSP, USGSG, and SDSU domains, respectively. The red triangles illustrate the stations for which the velocity is displayed in Figure A3.

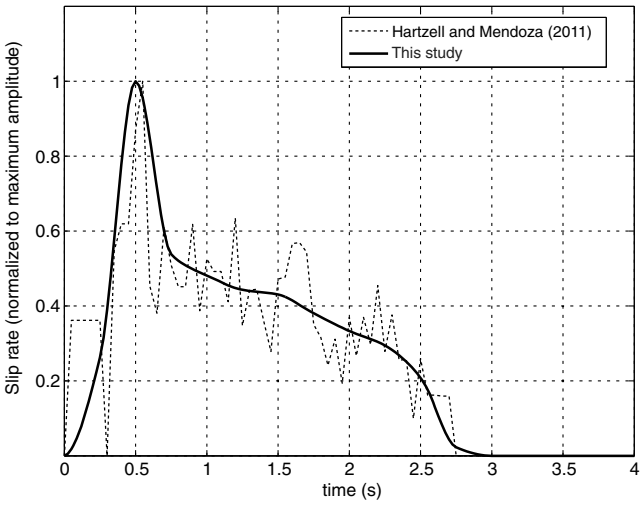

Figure A2. Slip rate function of the 2008 Mount Carmel earthquake used in the cross verification.

The domains used by each group, the location of the earthquake, and the stations used in the comparison are depicted in Figure A1. Specifications of each code are summarized in Table A1. The Central United States Velocity Model v.1.2 was used for the verification. The source time function used (Fig. A2) is a smoothed version of the inverted source in Hartzell and Mendoza (2011) for the Mount Carmel earthquake. The slip-rate function was filtered before running the simulation with a low-pass Butterworth filter with six poles, corner 0.5 Hz, and two passes (using the SAC command *lp butter npoles 6 corner 0.5 p 2*). Because the objective of the simulations was to verify that all platforms reproduced similar values, we constrained the resolution to a maximum of 0.5 Hz and minimum $V_S = 600$ m/s. All modelers produced 200 s of ground motion.

A visual comparison of selected stations of the signals obtained by the groups is displayed in Figure A3. The velocity waveforms of the two horizontal and the vertical components display qualitative agreement in shape, amplitude, and phase but reveal discrepancies as distance increases. All

Table A1
Characteristics of the Verification Simulations

Simulation Group	SDSU	USGSG	URSUSGSP
Domain			
Length (km)	373	390	264
Width (km)	555	520	600
Depth (km)	70	65	72
Southwest	−91.7000, 34.5461	−91.50000, 34.50000	−89.11472, 39.94140
Northwest	−91.6180, 39.5423	−91.63374, 39.18452	−86.35848, 38.90733
Northeast	−87.2827, 39.5237	−87.11942, 39.18452	−89.27891, 34.05854
Southeast	−87.3657, 34.5215	−87.25317, 34.50000	−91.90015, 35.02830
Projection	UTM	Bilinear	Spheroidal
Discretization			
Space	Staggered-grid FD Fourth order	Octree-based FE Second order	Staggered-grid FD Fourth order
Time	Second order	Second order	Second order
Resolution			
Cell or element size	200 m	Variable	250 m
F_{max} (Hz)	0.5	0.5	0.5
Minimum V_S (m/s)	600	600	600
Points Per wavelength	6	10	5
Attenuation			
Type	Coarse grained	Rayleigh	Coarse grained
Q_S	$0.300V_S - 100$ $600 \le V_S \le 1000$ $0.167V_S + 33$ $1000 \le V_S \le 4000$ 700 $4000 \le V_S$	-	$0.300V_S - 100$ $600 \le V_S \le 1000$ $0.167V_S + 33$ $1000 \le V_S \le 4000$ 700 $4000 \le V_S$
Q_P	$2Q_S$	-	$2Q_S$
Q	-	$0.300V_S - 100$ $600 \le V_S \le 1000$ $0.167V_S + 33$ $1000 \le V_S \le 4000$ 700 $4000 \le V_S$	-
Absorbing Boundaries			
Type	Perfectly matched layers	Lysmer–Kuhlemeyer	Clayton–Engquist

SDSU, San Diego State University or Olsen and Zhong; USGSG, U.S. Geological Survey Golden, Colorado, office or Ramirez-Guzman *et al.*; URSUSGSP, URS Corporation and U.S. Geological Survey Pasadena, California, office or Graves *et al.* V_S is given in meters/second.

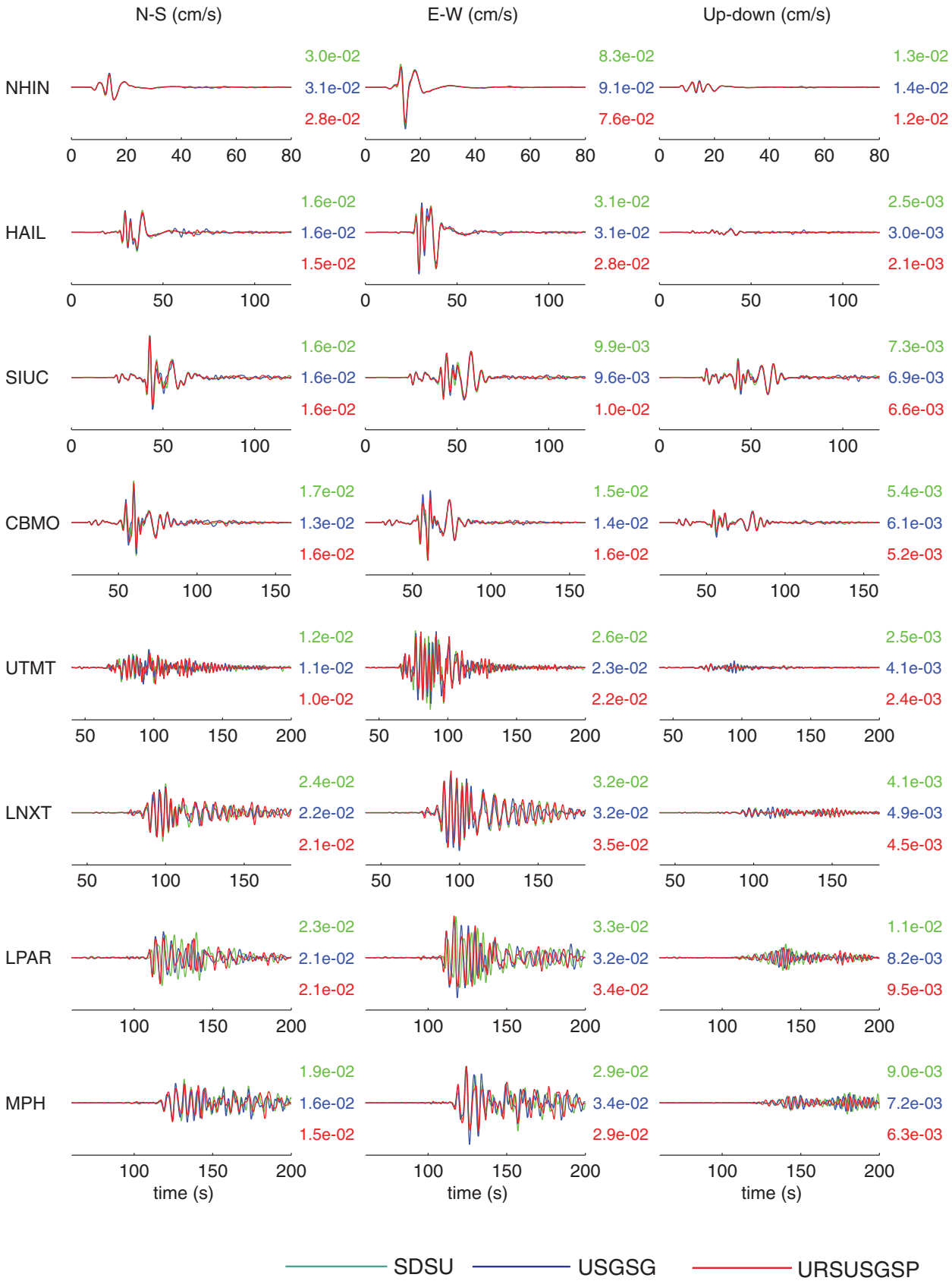

Figure A3. Waveform comparison. Ground-motion velocity synthetics are ordered as a function of epicentral distance. Red, blue, and green traces correspond to URSUSGSP, USGSG, and SDSU synthetics, respectively. Peak values per modeler are displayed (S-N, south–north; W-E, west–east).

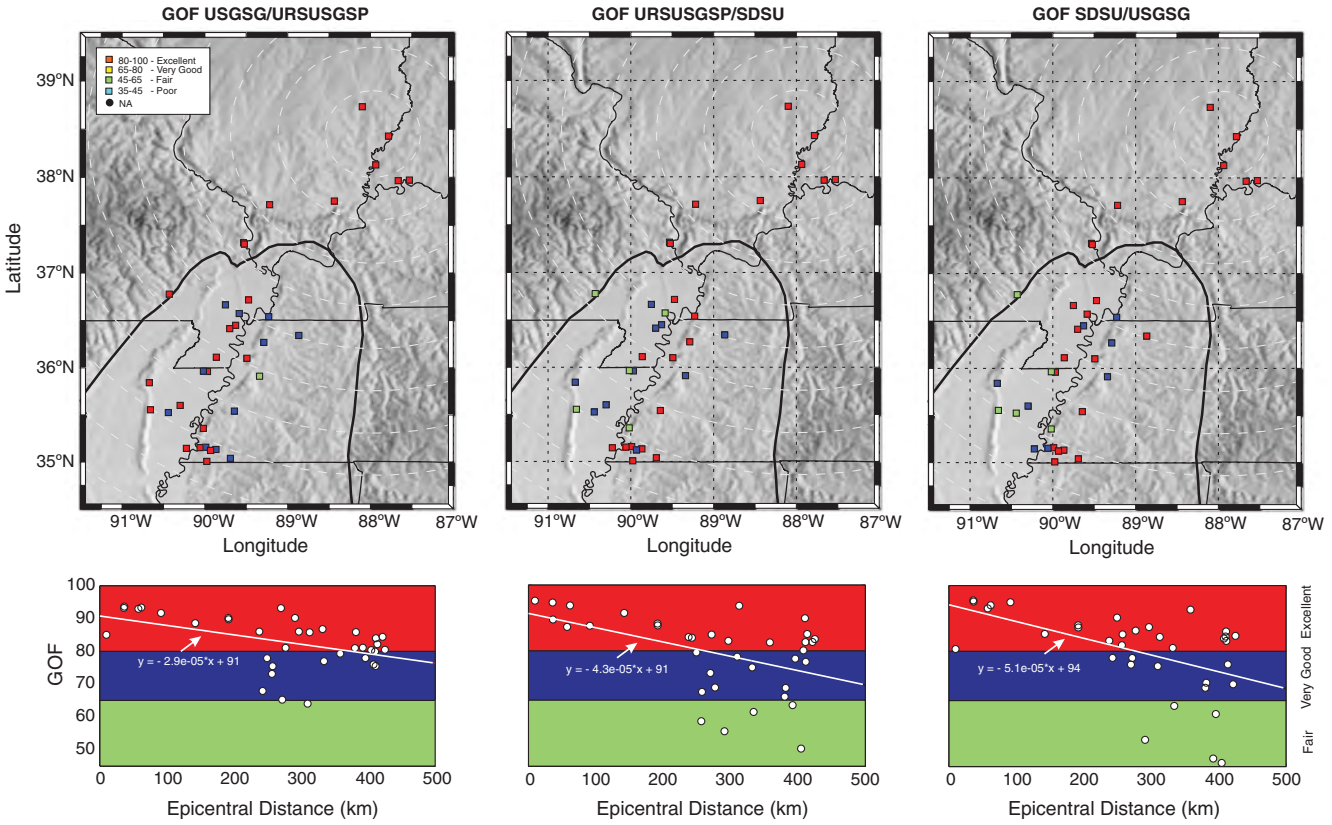

Figure A4. Goodness-of-fit (GOF) comparison following Olsen and Mayhew (2010). Each GOF comparison uses the grading scheme indicated in the figure, using as reference URSUSGSP, SDSU, and USGSG against USGSG, URSUSGSP, and SDSU, respectively. The lower panels show the same information as a function of epicentral distance.

codes reproduce the early phases equally well, even at long distance, but differ in the surface waves, most likely due to differences in the discretization of the material properties and damping mechanism implementation as well as the expected numerical dispersion due to the properties of the finite-difference and finite-element methods.

In addition, we performed a GOF between pairs of simulation groups (i.e., San Diego State University [SDSU] vs. U.S. Geological Survey Golden [USGSG], SDSU vs. URS Corporation and U.S. Geological Survey Pasadena [URSUSGSP], and URSUSGSP vs. USGSG), similar to the Olsen and Mayhew (2010) proposal for the 2008 M_w 5.4 Chino Hills, California, event. The GOF is defined as

$$\mathrm{GOF} = 100 \cdot \mathrm{erfc}\left(2\frac{p_{Sa} - p_{Sb}}{p_{Sa} + p_{Sb}}\right), \qquad \text{(A1)}$$

in which erfc is the complementary error function and p_{Sa} and p_{Sb} are the synthetic parameters for the simulation groups a and b (either USGSG, SDSU, or URSUSGSP), respectively. The quality of the fit among synthetic signals follows the scale proposed by the same authors: $80 \le \mathrm{GOF} \le 100$ as excellent, $65 \le \mathrm{GOF} < 80$ as very good, $45 \le \mathrm{GOF} < 65$ as fair, $35 \le \mathrm{GOF} < 45$ as poor but acceptable, and less than 35 as not acceptable.

We considered eight parameters from those recommended by Olsen and Mayhew (2010) to characterize the fit:

1. peak ground displacement (PGD);
2. peak ground velocity (PGV);
3. peak ground acceleration (PGA);
4. cumulative energy, defined as

$$E_i = \int_0^{t_d} v_i^2(\tau)d\tau, \qquad \text{(A2)}$$

in which t_d is 200 s and v_i is particle velocity in the direction i;

5. duration of the intense phase, defined as the time to reach from 5% to 75% E_i;
6. response spectral accelerations (SA) with a damping ratio of 5% and T centered at the frequency band under consideration;
7. mean velocity Fourier spectral (FS) amplitudes in the frequency band under consideration; and
8. cross correlation, defined as

$$Xcor = 100\max\left(\frac{\sum_{i=1}^{N}(x_i y_i)}{\sqrt{\sum_{i=1}^{N} x_i^2}\sqrt{\sum_{i=1}^{N} y_i^2}}, 0\right). \qquad \text{(A3)}$$

We calculated the GOF values for each of the parameters in the 0.05–0.45 frequency band for the three possible pair

combinations of the three simulation groups, that is, SDSU versus USGSG, SDSU versus URSUSGSP, and URSUSGSP versus USGSG. Then a station GOF per pair, henceforth GOFs, is found by computing the mean of all GOF parameters per station analyzed. Figure A4 displays the GOFs at each station, which reveals that the GOFs are within the very good-to-excellent range and is excellent in all combinations for stations outside the Mississippi embayment. On average, the poorest fits are found at the greatest source–station distances (e.g., >250 km), where differences in the elastic attenuation and implementation of media averaging cause larger variation in the GOF values. The smallest GOF values at these distances are mainly controlled by the cross-correlation metric, as determined by disaggregating the contributions from the GOF components. Differences in PGA, PGV, and SAs are much smaller, providing confidence in the NMSZ simulation results presented in this article.

In addition, and only as a reference, we include in the Ⓔ electronic supplement a comparison of the synthetic seismograms generated by the three groups and the observed records (see Data and Resources) at the same stations displayed in Figure A3. Note that such a comparison can only be taken as a reference because the verification does not include low-velocity materials that would have an impact on the results. A detailed comparison using a slightly modified model of the central United States is presented in Ramirez-Guzman *et al.* (2012), in which low velocities and higher frequencies were considered.

Instituto de Ingeniería
Coordinación de Ingeniería Sismológica
Universidad Nacional Autónoma de México
Avenida Universidad No. 3000
Coyoacán, México D.F. 04510
LRamirezG@iingen.unam.mx
(L.R.-G.)

U.S. Geological Survey
525 South Wilson Avenue
Pasadena, California 91106
(R.W.G.)

San Diego State University
Department of Geological Sciences MC-1020
5500 Campanile Drive
San Diego, California 92182-1020
(K.B.O., J.Z.)

U.S. Geological Survey
Denver Federal Center
Box 25046, MS 966
Denver, Colorado 80225
(O.S.B., S.H., R.A.W.)

Center for Earthquake Research and Information (CERI)
University of Memphis
3890 Central Avenue
Memphis, Tennessee 38152-3050
(C.C.)

URS Corporation
915 Wilshire Boulevard
Suite 700
Los Angeles, California 90017-3437
(S.N., P.S.)

Manuscript received 4 November 2014;
Published Online 28 July 2015